



NRC Publications Archive Archives des publications du CNRC

Experimental and computational investigations of flapping wings for Nano-air-vehicles

Yuan, Weixing; Lee, Richard; Levasseur, Luc

This publication could be one of several versions: author's original, accepted manuscript or the publisher's version. /
La version de cette publication peut être l'une des suivantes : la version prépublication de l'auteur, la version
acceptée du manuscrit ou la version de l'éditeur.

For the publisher's version, please access the DOI link below. / Pour consulter la version de l'éditeur, utilisez le lien
DOI ci-dessous.

Publisher's version / Version de l'éditeur:

<https://doi.org/10.1080/19942060.2015.1004820>

Engineering Applications of Computational Fluid Mechanics, 9, 1, pp. 199-219,
2015-04-01

NRC Publications Record / Notice d'Archives des publications de CNRC:

<https://nrc-publications.canada.ca/eng/view/object/?id=72e8bec0-4a62-4ee9-887e-ad10d42a2920>

<https://publications-cnrc.canada.ca/fra/voir/objet/?id=72e8bec0-4a62-4ee9-887e-ad10d42a2920>

Access and use of this website and the material on it are subject to the Terms and Conditions set forth at

<https://nrc-publications.canada.ca/eng/copyright>

READ THESE TERMS AND CONDITIONS CAREFULLY BEFORE USING THIS WEBSITE.

L'accès à ce site Web et l'utilisation de son contenu sont assujettis aux conditions présentées dans le site

<https://publications-cnrc.canada.ca/fra/droits>

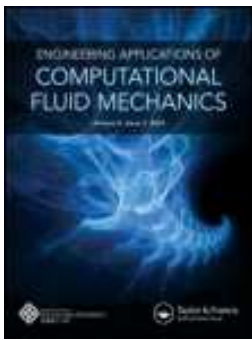
LISEZ CES CONDITIONS ATTENTIVEMENT AVANT D'UTILISER CE SITE WEB.

Questions? Contact the NRC Publications Archive team at

PublicationsArchive-ArchivesPublications@nrc-cnrc.gc.ca. If you wish to email the authors directly, please see the
first page of the publication for their contact information.

Vous avez des questions? Nous pouvons vous aider. Pour communiquer directement avec un auteur, consultez la
première page de la revue dans laquelle son article a été publié afin de trouver ses coordonnées. Si vous n'arrivez
pas à les repérer, communiquez avec nous à PublicationsArchive-ArchivesPublications@nrc-cnrc.gc.ca.





Experimental and computational investigations of flapping wings for Nano-air-vehicles

Weixing Yuan, Richard Lee & Luc Levasseur

To cite this article: Weixing Yuan, Richard Lee & Luc Levasseur (2015) Experimental and computational investigations of flapping wings for Nano-air-vehicles, Engineering Applications of Computational Fluid Mechanics, 9:1, 199-219, DOI: [10.1080/19942060.2015.1004820](https://doi.org/10.1080/19942060.2015.1004820)

To link to this article: <http://dx.doi.org/10.1080/19942060.2015.1004820>



© 2015 Crown in the Right of Canada.
Published by Taylor & Francis.



Published online: 01 Apr 2015.



Submit your article to this journal [↗](#)



Article views: 619



View related articles [↗](#)



View Crossmark data [↗](#)

Experimental and computational investigations of flapping wings for Nano-air-vehicles

Weixing Yuan*, Richard Lee and Luc Levasseur

Aerospace Portfolio, National Research Council (NRC) Canada, Ottawa, Ontario, K1A 0R6, Canada

(Received 14 June 2014; final version received 27 November 2014)

This paper presents the finalized results of a recent project which investigated the aeromechanical aspects of aerodynamic force generation by making use of flapping wings. Flapping-wing experiments using small wings have some unique challenges posed by the low force level (~ 1 N) and the cyclic wing motion. A tailored experimental water tunnel facility was developed for flapping wings operating at high reduced frequency with a complex two-dimensional and a three-dimensional motion profile. The experimental capability is demonstrated by the test cases of two-dimensional and three-dimensional flapping wings, designed according to a proposed notional nano-air-vehicle at a hovering condition. The features of the water tunnel, the geometric and kinematic parameters of the airfoils/wings, and the setups of the motion rigs for each test case are described. Measured forces and particle image velocimetry data are analyzed and cross-checked with the numerical results obtained from a code developed in-house. The comparisons of the experimental and numerical results show that the established experimental approach obtained a quantitatively reliable solution for the development of flapping wings and can serve for numerical validation of engineering tool developments. The investigation reveals that the kinematics of a rigid airfoil or wing is the dominant influence in the generation of aerodynamic forces, while the cross-section profile plays a secondary role. An asymmetric-wake-in-time is found behind the single airfoils and wings, which contributes to an asymmetry behavior of the resulting aerodynamic forces. In addition to the findings of single airfoils and wings, further analyses of the numerical and experimental results confirm that wing-wing interaction through the clap-fling mechanism can intensify the generation of the thrust force while accompanied by a small reduction in the overall propulsion efficiency.

Keywords: flapping wing; low Reynolds number flow; micro air vehicle; water tunnel; computational fluid dynamics

Nomenclature

b	= length of the wing span	U_{ref}	= reference velocity, $U_{ref} = \ U_{\infty} + V_{induced}\ $
$C_D(C_d)$	= drag coefficient based on reference area and reference velocity, $C_D = F_x / \frac{1}{2}\rho U_{ref}^2 s$	U_{∞}	= freestream velocity
$C_L(C_l)$	= lift coefficient based on reference area and reference velocity, $C_L = F_y / \frac{1}{2}\rho U_{ref}^2 s$	u, v, w	= velocity components
C_p	= pressure coefficient, $C_p = (p - p_{\infty}) / \frac{1}{2}\rho U_{ref}^2$	$V_{induced}$	= peak velocity of the plunging/flapping motion, $V_{induced} = H\omega$ or $V_{induced} = 0.5b\Gamma\omega$
c	= airfoil chord length	x, y, z	= Cartesian coordinates
F_x, F_y	= forces in the x- and y-directions	x_0	= pivot location
f	= frequency of the flapping motion	α	= effective angle of attack, positive nose-up
H	= plunging amplitude (peak value) of the point about which the airfoil pitches	δ	= phase difference between pitching and plunging (90 degs for this study)
\bar{H}	= normalized plunging amplitude, $\bar{H} = H/c$	Γ	= amplitude (peak value) of the root flapping angle
h	= plunging displacement of the point about which airfoil pitches	γ	= flapping angle of the leading edge about which the airfoil pitches
k_c	= reduced frequency, $k_c = \pi fc / U_{\infty}$	μ	= fluid dynamic viscosity
Re	= Reynolds number based on airfoil chord, $Re = U_{ref} c / (\mu/\rho)$	Θ	= pitching amplitude (peak value)
s	= projection area of the wing body	θ	= pitching displacement (angle) of the airfoil, positive nose-down (tail-up)
T	= period of the flapping motion	θ_0	= mean pitch position (zero for this study)
t	= time	ρ	= fluid density
		ω	= angular frequency of the flapping motion, $\omega = 2\pi f$
		ω_z	= spanwise vorticity, $\omega_z = \frac{\partial v}{\partial x} - \frac{\partial u}{\partial y}$

*Corresponding author. Email: weixing.yuan@nrc-cnrc.gc.ca

1. Introduction

The concept of a new class of air vehicle is emerging amid the progress in technological areas such as aerodynamics, micro-electronics and sensors, micro-electromechanical systems, and micro-manufacturing methods. Referred to as a “nano-air-vehicle” (NAV), its mission will typically be to penetrate and reconnoitre confined spaces without being detected, most likely in an urban environment. To complete this mission successfully, the vehicle will be required to hover steadily and quietly, perch, maneuver with ease and swiftness, and be responsive to sudden disturbances such as gusts, which are inevitable in the urban setting. Such vehicles are envisioned to be small in size, being less than 7.5 cm in length typically, with a mass of less than 10 grams. Satisfying the demanding mission requirements with a conventional fixed-wing/forward-thrust platform, or a rotary-wing approach, seems unlikely because the aerodynamics of these vehicles provides less propulsive efficiencies at a small scale (Young, 2005). Insect flight, on the other hand, offers an attractive alternative solution. Insects and tiny birds, such as hummingbirds, are small airborne bodies which rely on the unsteady aerodynamics of flapping wings to produce lift and thrust. The unsteadiness of the aerodynamics arises from the rapid complex motion of wings – which flap and rotate through large angles, and sweep fore and aft at the same time – combined with rapid adjustments of the shape of the wing. Developing an understanding of the kinematics of insect wings and the aerodynamics arising from the motion are essential toward the development of an engineering tool capable of rapidly optimizing the design and motion of a wing set for a nano-air-vehicle.

A great deal of progress has been made in the past decade in understanding the flapping-wing aerodynamics. Mueller (2001), Shyy, Lian, Tang, Viieru, and Liu (2008), Platzer, Jones, Young, and Lai (2008) and Ol (2010) provided broader collection and detailed review of previous research work in flapping-wing aerodynamics at very low Reynolds numbers. It was first recognized by Knoller (1909) and Betz (1912) that a flapping airfoil generates thrust. Thrust generation is crucial for insect-like and NAV flights, in particular at hovering conditions – a primary topic of the present study. Of fundamental and applied interest, Lai and Platzer (2001) visualized that a finite thrust was generated due to the vortex shedding from the trailing edge of a NACA 0012 airfoil in pure plunging motion at zero freestream velocity. Back to 1990, Freymuth (1990) visualized the flow past an airfoil in combined harmonic plunging and pitching motion in still air and revealed strong vortices shed from both leading and trailing edges that organize efficiently into a jet structure and hence produce a large thrust. Sunada, Kawachi, Matsumoto, and Sakaguchi (2001) used a load cell with strain gages to measure the instantaneous forces acting on a two-dimensional (2D) wing undergoing a combined pitch–plunge motion and determined the combinations of these

forces for maximum time-averaged thrust and for maximum efficiency. Although 2D models showed advantages in elucidating conical vortices forming on the leading and trailing edges, three-dimensional (3D) models are needed to cover the spanwise flow features thus understand thoroughly the physics of force generation by hovering insects. Since complexities of flow visualizations in 3D experiments, computational fluid dynamics (CFD) tools showed complementary effectiveness. Back in the 1990s, Liu, Ellington, Kawachi, van Den Berg, and Willmott (1998), Liu & Kawachi (1998) had initiated CFD simulations of hawkmoth hovering. In these simulations, the artificial compressibility method following (Chorin, 1968) was used by adding a pseudo-time derivative of pressure to the continuity equation. Yuan, Khalid and Huang (2008) attempted 3D flow simulations past an insect-like wing which was similar to the ones used by Dickinson, Lehmann, and Sane (1999) and Sane and Dickinson (2001). Young, Lai, and Germain (2008) investigated the effect of flapping amplitude, flapping frequency, and wing rotation timing and duration on the aerodynamic performance of the dragonfly hind wing using a 3D Navier–Stokes solver. It was found that the mean vertical force and power are essentially independent of frequencies exceeding 5 Hz and the hovering efficiency peaks at a flapping amplitude of about 35 deg, very close to the observed amplitude of the dragonfly hind wing in hover. More recently, Fairuz, Abdullah, Yusoff, and Abdullah (2014) investigated the fluid-structure interaction of unsteady aerodynamics of a flapping wing at a low Reynolds number.

Although there exists a large body of experimental work on flapping-wing aerodynamics and they provide good qualitative or even quantitative descriptions, because of the difficulties associated with doing experiments on low force level (~ 1 N) and the complex flapping motion, the reported quantitative results are often incomplete or hard to be used for engineering applications. A collaboration involving Defence Research and Development Canada in Valcartier (DRDC-V), Advanced Subsonics Inc. (ASI), and the Aerodynamics Laboratory of the National Research Council Canada (NRC-Aerospace), has been investigating flapping-wing aerodynamics for NAV applications. The immediate goal of the collaboration was to develop the means to optimize rapidly the wing design and motion of a notional NAV (Figure 1) and, in turn, develop an optimized configuration; in the long term, the collaboration envisioned building a functional prototype in stages. The work of the collaboration was introduced by Lesage et al. (2008). The progress of NRC-Aerospace concerning its CFD contribution has been reported subsequently by Yuan and Khalid (2008) and Yuan, Lee, Hoogkamp, and Khalid (2010). The detailed experimental setup and preliminary experimental results have been elaborated and presented by Lee, Yuan, Levasseur, and Hoogkamp (2011). This paper will continue to chronicle the collaboration, concentrating on the further analyses of experimental and

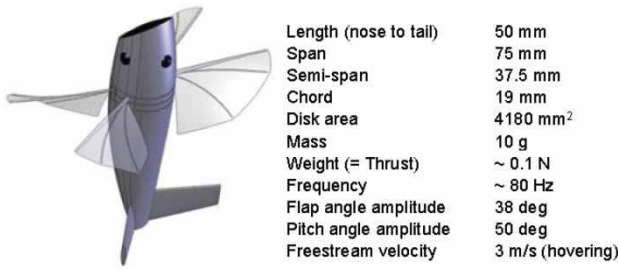


Figure 1. The notional nano-air-vehicle using the “clap-fling” mechanism. The wings flap about the central axis of the body and twist about the leading edge (Lesage et al., 2008; Zdunich, 2008).

numerical results, focusing on thrust generation and its related physics in hovering conditions.

Insects generate thrust and lift by controlling wing kinematics that includes flapping motion during stroke cycles. To facilitate the investigation, two standard test cases, based on a notional NAV, are defined in this study: a plunging and pitching two-dimensional airfoil (2D test case), and a flapping and pitching three-dimensional wing (3D test case). These test cases, including the described kinematics, are easy to follow numerically or even experimentally. The flapping-wing experiments using small wings as in the present study have unique challenges posed by the low force level (~ 1 N) and the complex wing motion. The low force levels required careful design and calibration of the load cells and motion control system. After detailed description of the experimental procedure, combined experimental and computational analysis is further performed. The results generated by the CFD codes are validated by experimental results produced from water tunnel tests of the standard test cases at NRC-Aerospace; in turn, CFD results provide detailed insights in flow physics for cross-check of the experimental data. In addition to the further analyses of the finalized results of the single flapping airfoils and wings, the paper will present the contributions on multi-wing interaction known as the clap-fling effect (Ellington, 1984; Weis-Fogh, 1973). These results could help calibrations of panel codes as engineering tool to optimize wing shape and motion with rigid or flexible wings for NAVs (Yuan et al., 2010; Zdunich, 2010).

2. Standard test cases for the notional NAV

A notional NAV was developed by the collaboration team to provide a context for vehicle size, motion characteristics, and performance parameters, and to serve as a starting point for the optimization process (Lesage et al., 2008; Zdunich, 2008). The definition of the vehicle was based on the mission requirements, anticipated progress in complementary technologies, and the experience gained from the development of the Mentor micro-air-vehicle (MAV), which flew successfully in March 2002 (Zdunich et al., 2007). Similar to the Mentor, the wings of the notional

Table 1. Summary of scaling parameters and model kinematics and geometry for the water tunnel test cases.

		2D	3D
Scaling parameter	Reduced frequency	1.59	1.59
	Amplitude-to-chord ratio	0.75	1.0
	Induced Reynolds number	9,500	14,300
Model kinematics	Frequency	0.5 Hz	0.46 Hz
	Plunge/flap amplitude	48 mm	15 degs
	Pitch amplitude	30 degs	40 degs
	Freestream velocity	64 mm/s	64 mm/s
Model geometry	Reference chord	64 mm	70 mm
	Airfoil/wing thickness	3.18 mm	3.18 mm
	Semi-span		350 mm

NAV flap in a three-dimensional manner (Figure 1). The wing is finite and the wing tip sweeps farther and faster than the wing root.

The flapping mechanism is a single degree-of-freedom (1-DOF) actuation mechanism, which is light and robust because the mechanism is not overly complicated. The notional NAV possesses a four-wing “double hummingbird” configuration and takes advantage of the clap-fling mechanism to obtain an improved thrust-to-power ratio and a high thrust for a limited disk area. In addition, the notional vehicle also possesses other features including thin flat wings, passive aeroelastic-tailoring of wing camber and span-dependent twist.

Having developed a concept for a full-scale NAV, the similitude parameters can be developed subsequently for the standard test cases suitable for the NRC water tunnel. The standard test cases consider a hovering condition. Although the ground velocity of the vehicle is zero, the freestream velocity (3.0 m/s) is estimated according to the induced slipstream behind the flapping wings based on the actuator disk theory. The similarity parameters for dynamic, kinematic, and geometric scaling are, respectively, Reynolds number, reduced frequency, and flap-amplitude to chord ratio (Table 1). Of the three scaling parameters, only the matching of Reynolds number is relaxed.

The flap-amplitude to chord ratio (H/c) is an important geometrical similarity parameter for flapping wing flight. The value of this ratio is determined at approximately 77% of the wing semi-span, measured from the flap axis. This location is arbitrarily chosen as representative of the main “working” portion of the wing. For the standard 3D test case, H/c for the notional NAV is approximately 1.0. For the 2D test case, however, H/c was reduced to 0.75 because the motion rig was unable to produce sufficient plunge amplitude to render $H/c = 1.0$. $H/c = 0.75$ corresponds to that at 58% of the semi-span of the notional NAV.

2.1. Standard 2D test case

To facilitate the understanding of the flow physics in the early going, the 2D case imposes two-dimensional flow over an airfoil and simplifies the flapping motion of the NAV by transforming its rotational motion to linear motion, i.e., plunge. The 2D test case was developed well suited for the water tunnel and its motion rig.

The instantaneous position of the airfoil is expressed as a linear superposition of motion due to plunging (translation) and that due to pitching (rotation) (Figure 2). The motion in both pitch and plunge is assumed to be harmonic. The airfoil pitches about its leading edge, which is consistent with a passively twisted wing of the type envisioned for the notional nano-air-vehicle. The position due to plunging is given by:

$$h(t) = H \sin(\omega t + \delta), \quad (1)$$

where H is the plunging amplitude and $\omega = 2\pi f$ is the circular frequency. The pitching motion of the airfoil is described by:

$$\theta(t) = \theta_0 + \Theta \sin(\omega t), \quad (2)$$

with a positive angle when pitching counter-clockwise as illustrated in Figure 2. In this study, $\theta_0 = 0$ degs. and $\Theta = 30$ degs. A phase angle of $\delta = 90$ degs was selected because it was found to produce good results during the Mentor program (Zdunich et al., 2007), as well as by researchers of larger-scale flapping-wing vehicles (DeLaurier, 1993a, 1993b).

The counter-clockwise direction for the pitch angle was arbitrarily defined although it provided convenience in coding and thus was adopted by some researchers, e.g. Guglielmini & Blondeaux (2003) in polar coordinate system and Zdunich (2008) for a panel code. However, it did not alter the conventional definition of the aerodynamic angle of attack that is positive in clockwise direction. The

instantaneous angle of attack can be expressed as:

$$\alpha(x, t) = -\theta(t) - \tan^{-1} \left[\frac{\dot{h}(t) + \dot{\theta}(t)(x - x_0) \cos(\theta)}{U_\infty + \dot{\theta}(t)(x - x_0) \sin(\theta)} \right], \quad (3)$$

where \dot{h} and $\dot{\theta}$ are the first time-derivatives of Equations 1 and 2, respectively. The terms in the brackets in Equation 3 represent the contributions induced by the plunging motion and the pitching oscillation, respectively, which causes an equivalent cambered wing effect (Yuan & Khalid, 2008). In this work, the pivot point is the leading edge; thus $x_0 = 0$. The instantaneous angle of attack at the leading edge, as described by Equation 3, is plotted in Figure 3. To help readers compare with the predictions of thin airfoil theory or panel methods, the effective angle of attack as defined by the three-quarter chord is also plotted in the figure.

Given a reference length and a reference velocity, one can define the Reynolds number. In forward flight, the freestream velocity is often used as the reference velocity. For the 2D case, the small freestream velocity results in a Reynolds number $Re_\infty = \rho U_\infty c / \mu = 4 \times 10^3$ and the reduced frequency is $k_c = \omega c / 2U_\infty = 1.59$. In hovering, the wing tip velocity may be used as the reference velocity (Shyy et al., 2008). Identifying the peak velocity of the plunging motion as $V_{induced} = H\omega$, the induced Reynolds number and the reduced frequency could be recovered as $Re_f = \rho V_{induced} c / \mu = 9.5 \times 10^3$ and $k_{induced} = \omega c / 2V_{induced} = 0.67$, respectively. Since the speed of the airfoil/wing due to flapping may be very large compared to the freestream velocity, especially near the hover condition as in this study, a generalized Reynolds number based on a combination of these two velocities is used:

$$Re = \frac{\rho \|U_\infty + V_{induced}\| c}{\mu}. \quad (4)$$

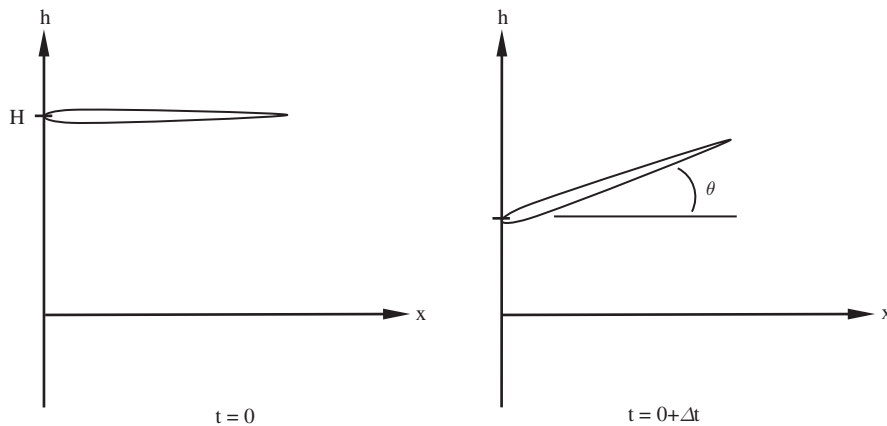


Figure 2. Schematic of the airfoil in plunging and pitching motion.

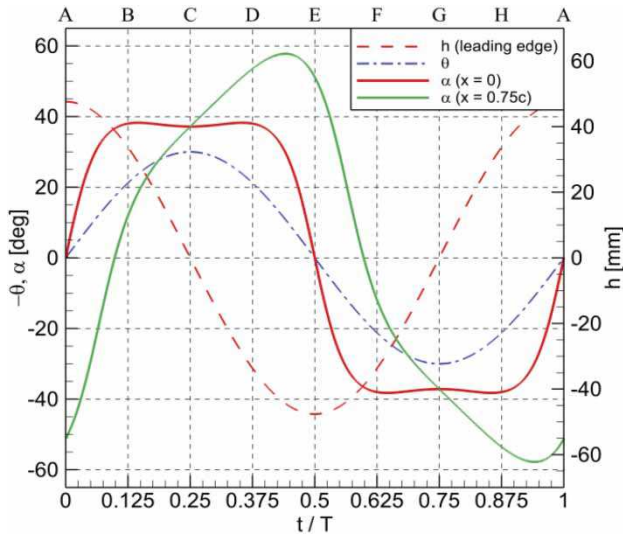


Figure 3. Time history of the effective angle of attack in accordance with the airfoil plunging and pitching motion.

As a result, the generalized Reynolds number of the 2D test case is $Re = 10.5 \times 10^3$. This practice had been employed by some researchers in the flapping-wing community. Zdunich (2008) used the magnitude of the vector sum of the freestream velocity and the velocity due to airfoil plunging as reference velocity to nondimensionalize the forces and moments. In fact, this reference velocity was termed as the relative inflow by Azuma, Okamoto, and Yasuda (2001) and relative velocity of the airfoil through the fluid by Hall, Pigott, and Hall (1997) and Hall and Hall (2001). Since all resulted Reynolds numbers using the three different reference velocities are listed here, one can easily rescale the nondimensional parameters for individual preference.

2.2. Standard 3D test case

The test case parameters are listed in Table 1. The flapping amplitude is limited to 15 degs because of the constraint by the width of the test section. A schematic of the wing model is shown in Figure 4. The model is tapered both in planform and thickness. The radius of flapping rotation is geometrically representative of the NAV. In order to avoid free surface effects, some clearance between the root of the wing and the surface of the water was deemed necessary.

Similar to the 2D case, the position of the wing at any time is expressed as a linear superposition of motion due to flapping and pitching, which are both rotational motions and assumed to be harmonic. The wing also pitches about its leading edge. The position due to flapping is described by:

$$\gamma(t) = \Gamma \sin(\omega t + \delta). \quad (5)$$

As in the 2D test case, the pitching motion lags the flapping motion by a phase angle of 90 degs. The description of the pitching motion of the wing is identical to Equation 2.

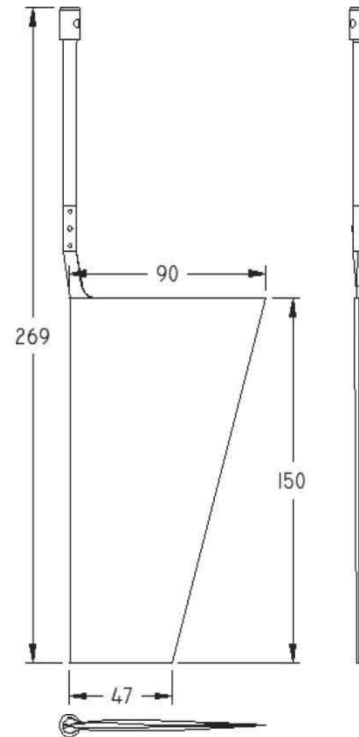


Figure 4. A schematic of the 3D wing model featuring a tapered NACA 0005 cross-section. The CFD simulation did not model the supporting arm. The dimensions are expressed in millimeters.

The setup results in a generalized Reynolds number based on the reference chord: $Re = 19 \times 10^3$.

3. Description of the experimental setup

The standard test cases were carried out experimentally in the Eidetics Flow Visualization Water Tunnel at NRC-Aerospace (Figure 5). The water tunnel features an open-surface test section with a return circuit. The nominal dimensions of the test section are 38 cm wide, 51 cm high, and 163 cm long. The maximum freestream velocity achievable in the test section is 305 cm/s; 20% of this range was required for the standard test cases. The freestream turbulence intensity in the test section is rated at less than 1%. Even so, dye flow visualization revealed that fluctuations in the test section increased after approximately 240 seconds of continuous operation of the facility. The increased fluctuations were attributed to remnants of the turbulent wake, which was developed by the large amplitude plunge motion of the 2D airfoil model but not attenuated adequately by the return circuit or the flow conditioner elements in the delivery plenum. For this reason, the operation of the motion rigs and the measurement of load data were limited to 180 seconds for both the 2D and 3D test cases.



Figure 5. The water tunnel at NRC-Aerospace with the two-axis motion system installed.

3.1. Standard 2D test case

The experimental setup for the standard 2D test case is illustrated in Figure 6. As mentioned earlier, Lai and Platzer (2001) visualized that a finite thrust was generated due to the vortex shedding from the trailing edge of a NACA 0012 airfoil in pure plunging motion at zero freestream velocity. However, Guglielmini and Blondeaux (2003) showed that an elliptic airfoil generated zero time-averaged thrust due to the symmetry of the resulting flow. To confirm possible airfoil effects in this study, two rigid 2D airfoil models were designed and manufactured: one with a NACA 0005 cross-section; the other, a flat plate with a constant thickness equal the maximum thickness of the NACA 0005 airfoil. Both models featured a span of

25.4 cm and were fabricated from stainless steel to protect against corrosion and for stiffness, especially in the case of the NACA 0005 model which has a very thin trailing edge. Tall glass endplates were placed carefully at both tips of a model to mitigate tip effects and to encourage two-dimensional flow conditions over the airfoil; a nominal clearance of 1 mm was maintained between an endplate and the model, throughout its motion profile. The open surface above the airfoil was removed with the installation of a large plate just below the waterline; centered over the model, the plate was approximately five chords long and its width covered the test section. Reflection planes – appearing above and below the 2D airfoil model in the figure – are available for simulating the clap-fling phenomena mimicking multiwing interaction in a simplified way.

The motion of the airfoil model is controlled by a two degree-of-freedom (2-DOF) system. The model is connected, at its spanwise center, to a pair of vertical plunge rods. Each plunge rod is driven by a linear shaft motor integrated with a slider system; a linear encoder conveys the position of the motor to the motion controller, closing the feedback loop. The linear motion of the plunge rods is programmed to provide the sinusoidal plunge and pitch motions at the frequencies and amplitudes prescribed by the test case. The deviation of the actual motion of the airfoil model from the prescribed kinematics was around 0.5% of the maximum amplitude, see Lee, Yuan, Levasseur, and Hoogkamp (2011).

Two uniaxial load cells – each with a rating of 44.5 N (10 lbs) – sensed the lift force developed by the airfoil

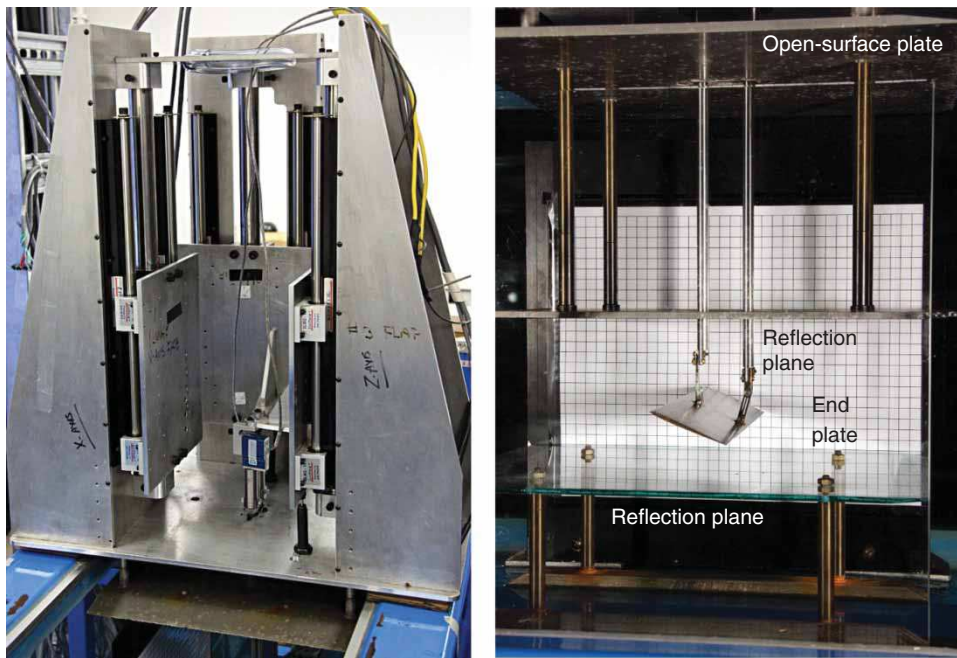


Figure 6. 2D model two-axis motion system. Left: the 2-DOF motion rig; Right: the two-dimensional airfoil model is shown between two reflection planes. The presence of the large plate seen at the top of the photograph removes the free surface condition above the airfoil model, when the reflection planes are not present.

and acting on the plunge rods. Each load cell was mounted inline between a plunge rod and its drive mechanism. The estimated uncertainty in the total lift force measurement is 0.084 N (8.6 g). The natural frequency of a plunge rod and load cell combination is 147 Hz. Drag force was not measured because the desired approach to acquire this quantity was not facilitated.

The output signals of the load cells and position encoders were sampled at rate of 1 kHz and acquired for 81 cycles of motion. Data were collected for both “wind” and “tare” conditions. The output analog signals of the load cells were filtered before conversion to a digital signal, and then digitally filtered once more with a low-pass cutoff of 10 Hz. The lift force signal was corrected for weight, inertial loading, and buoyancy. After the first six motion cycles were discarded – to account for transient flow conditions at the start of a run – the lift force data were parsed to formulate a three-cycle ensemble-average.

As mentioned, the tare scheme accounted for weight, inertial loading, and buoyancy. The lift force was adjusted by each tare component on a sample-by-sample basis. Unlike the practice of Isaac, Rolwes, and Colozza (2008) who used a numerical approach for calculating the inertia and gravity forces, the weight and inertial tares were acquired together experimentally by running the 2D model through the motion profile in a test section emptied of water. Care was taken to ensure that this tare signal was synchronized with its corresponding wind signal throughout the motion profile. A weight and inertial tare signal was acquired for each wind signal acquired. The buoyancy tare, on the other hand, was an analytical model which comprised the mean buoyancy force, estimated with the airfoil model placed at the zero-displacement plunge position; and a small fluctuating component, which increased or decreased the buoyancy tare as changes of the wetted volume of the plunge rods occurred during the motion profile.

Phase-locked particle imaging velocimetry (PIV) measurements of two components of velocity – streamwise and vertical – were performed for the 2D test case to identify features in the flow over the surface of the airfoil and in its wake. A LaVision PIV system was configured to receive a trigger signal from the motion control system; once triggered, images were acquired at intervals of 1/16 cycle to correspond with CFD results. The streamwise measurement plane was aligned with the quarter-span of the airfoil model; the laser illuminated the plane from beneath the test section. The airfoil model was coated with a Rhodamine-based paint to mitigate the reflection of laser light. The PIV recording parameters are listed in Lee et al. (2011).

3.2. Standard 3D test case

The experimental setup for the standard 3D test case is illustrated in Figure 7. Similar to the 2D airfoil mod-

els, two rigid 3D wing models were manufactured with a NACA 0005 and a flat plate cross-section. The models were fabricated from aluminium for lightness and shared an interchangeable supporting arm, which connected the wing model to the balance. The center of the cross-section of the supporting arm coincides with the leading edge of the wing model so that the pitching motion rotates the wing about the leading edge.

The sinusoidal motion prescribed for the wing model was controlled by a three degree-of-freedom (3-DOF) motion system that is capable of providing flapping, pitching, and sweeping motions directly. The sweeping motion was not activated for this work. Each motion was driven by a brushless DC servomotor equipped with a gear reduction box. An angular position encoder, integrated with the servomotor, closed the feedback loop for the motion control system. The difference between the prescribed kinematics of the wing model and the motion sensed by the encoders was less than 1% of the maximum amplitude (Lee et al., 2011).

A bi-fold five-component balance was mounted between the wing and the motion system, inline with the leading edge of the wing (Lee et al., 2011). The balance measured the normal and axial forces, and the pitching, rolling, and yawing moments in the body axes of the balance. The limit to which each component was calibrated, as well as the estimated measurement uncertainty and natural frequency are listed in Lee et al. (2011).

The acquisition and reduction of data – especially the adjustments for weight, inertial loading, and buoyancy in the force and moment data – followed the same procedures as for the standard 2D test case, described earlier. A difference between the procedures of the two test cases is the frequency cutoff of the low-pass digital filter; for the 3D test case, the cutoff was set to 2.3 Hz because 95% of the fluctuating component of normal force was captured below this frequency. All loading due to the supporting arm by itself was deemed negligible and was not considered in the data reduction process. The normal and axial forces were transformed into lift and drag forces in the test-section axes. The rolling and yawing moments were transferred from the resolving center of the balance to, respectively, the flapping axis and the intersection of the flapping and pitching axes in the 3-DOF motion rig; the transfer of the pitching moment was not necessary.

No PIV measurements were acquired for the 3D test cases.

4. Description of the in-house CFD solver

The computational-fluid-dynamics code, INSflow, was developed in-house at NRC-Aerospace for solving three-dimensional unsteady incompressible flows. The code has been used for a number of applications including large-eddy and unsteady Reynolds-averaged Navier–Stokes

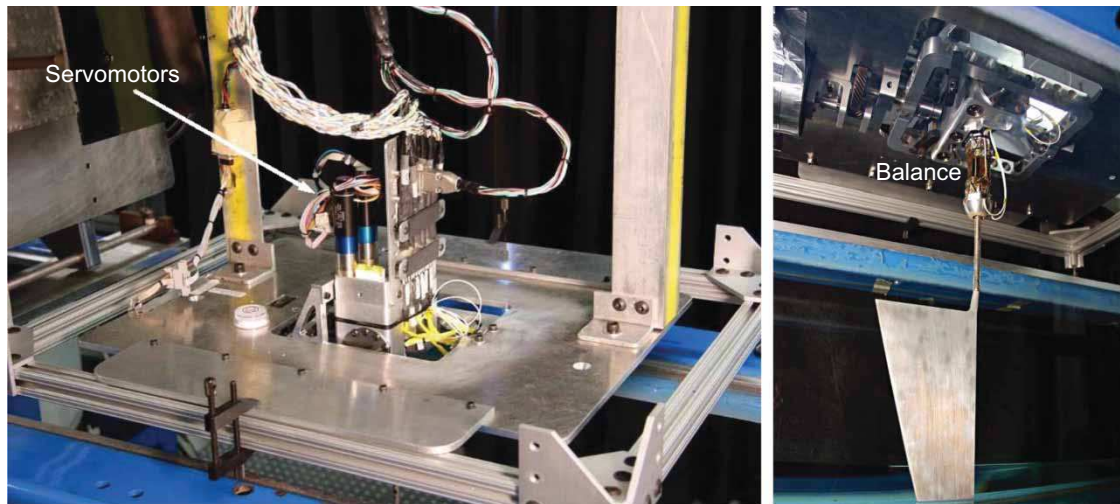


Figure 7. The 3-DOF motion rig. The three-dimensional wing model is installed in the balance.

simulations (Yuan, Poirel, Wang, & Benaissa, 2014), low-Reynolds flows (Yuan, Khalid, Windte, Scholz, & Radespiel, 2007), laminar-separation flutter (Yuan, Poirel, & Wang, 2013), and flapping-wing aerodynamics (Yuan et al., 2008, 2010).

INSflow applies the integral form of the conservation laws of mass and momentum. A fully implicit second-order temporal differencing scheme was implemented in the discretization, which made the algorithm stable for large timesteps. The discretization of the convective and diffusive fluxes was carried out in a co-located variable arrangement using a finite-volume approach that was second-order accurate in space. A first-order upwind scheme is available. The coupling of the pressure and velocity was handled using a modified SIMPLE algorithm (Ferziger & Perić, 1996; Patankar, 1980). The calculations were performed on moving grids; the velocity of the grid movement was included in the governing equations in an inertial frame of reference. In order to avoid artificial mass sources generated by the grid velocity, a space conservation law was introduced to ensure a fully conservative property in the computations, as applied by Demirdžić and Perić (1990).

4.1. Standard 2D test case

The 2D test case was considered a laminar flow. The 2D calculations were performed on O-type meshes. The farfield boundaries were located about 25 chords away from the surface of the airfoil. The nominal mesh had 481×129 grid points. This mesh was designed with a grid density increasing toward the wall at a rate of 6% for the near-wall region and 8.7% for the outer region. The grid lines in the normal-to-the-wall direction were simple straight lines. Improved grid orthogonality would accelerate the calculation convergence and increase the simulation accuracy, but the modification was not investigated in this

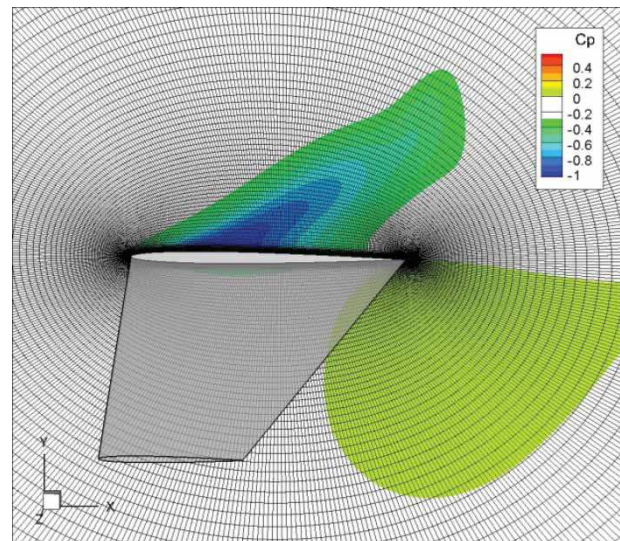


Figure 8. Computational mesh of the 3D NACA 0005 wing configuration in flapping motion.

study. The calculations were started from a stationary fluid. In general, the third cycle produced comparable results to the second cycle for the cases reported in this study.

To select a suitable grid for the investigations, computations for the standard 2D test case were conducted using second-order spatial discretization on three O-meshes: 241×97 , 481×129 , and 961×161 , with corresponding timesteps for one plunging cycle of 2888, 3840, and 5760, respectively. Eight flapping cycles were conducted for the coarse and medium grids. Only six cycles were completed for the fine mesh. The discrepancies of the results of the aerodynamic forces obtained on the three grids were minimal. The aerodynamic coefficients matched well starting from the second cycle (Yuan et al., 2010). Based on this observation, the results obtained from the medium grid will be discussed in this paper.

4.2. Standard 3D test case

Same as the 2D test case, the 3D test case was considered a laminar flow. A grid with $481 \times 129 \times 33$ nodes was used for the flow domain around the wing body (see Figure 8), with a farfield boundary located at about 25 reference chord lengths. This grid size is comparable to the medium grid used in the earlier 2D calculations, but with 33 stations located along the wing span. The computational domain contained two extensions. The first one stretched from the wing root to the flapping axis, while the second extended beyond the wing tip for 150 mm, which was equal to the spanwise dimension of the wing body. These two extended domains were discretized using grids with $481 \times 133 \times 33$ nodes, thus constituting a three-block structure. Compared with the grid around the wing body, there were four extra grid points in the direction normal to the flapping arm, to mesh the thickness of the wing root and tip surfaces.

In the calculations, the farfield and the spanwise boundaries were subject to a freestream condition. The calculations were initiated from a stationary state. The computations were found to be time consuming and no time convergence study was performed. Since the Reynolds number was close to the one in the 2D test case, as many as 384 timesteps per flapping cycle were used to discretize the governing equations in time, which was confirmed to be sufficient for obtaining major features of the flow physics in the timestep refinement for the 2D test case reported in Yuan et al. (2010). An upwind scheme was used for the discretization in space as the second-order scheme encountered numerical instabilities.

5. Experimental and computational results

Measured and computed forces and spanwise vorticity are presented for the standard 2D and 3D test cases. For the 3D test case, only forces are available because PIV measurements were not undertaken. The experimental results are reflective of a mean flow field, whereas the computed results are instantaneous. Most results are expressed in engineering units since we wish to illustrate, specifically, the small magnitude of the loading encountered.

5.1. Standard 2D test case

5.1.1. Lift force

Two cycles of lift measurements and lift predictions, produced by INSflow, are superimposed in Figure 9. The experimental results are taken from an ensemble-average of 24 three-cycle time-series; the CFD results are the last two instantaneous cycles from a series of eight computed cycles. Compared with the previous publications (Lee et al., 2011; Yuan et al., 2010), a slight discrepancy is seen in the experimental data, which rectifies an inaccuracy in the three-cycle ensemble-averaging. The motion profiles synchronized the presentation of the two sets of results.

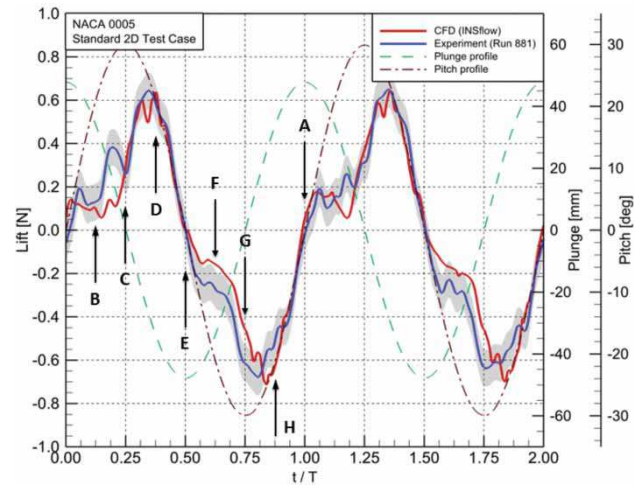


Figure 9. Measured and computed lift force for the pitching–plunging NACA 0005 airfoil. Standard 2D test case: $Re = 10.5 \times 10^3$, $U_\infty = 0.0635$ m/s, $f = 0.5$ Hz. The shaded band represents uncertainty in the lift measurement.

In general there is good agreement between the results; for instance, there is repeatable behavior corresponding with the pitching–plunging motion schedule; the magnitudes of peak lift match well; and there are no indications of obvious or significant phase shift. For the most part, the computed lift force falls within the uncertainty band of the measured lift force. The CFD simulation reproduces successfully the sluggish development of lift force at the start of both the downstroke and the upstroke. Interestingly, the magnitude of the lift forces at the upstroke and the downstroke differ slightly; the difference could be indicative of an interaction between the airfoil and its asymmetric wake, which will be discussed later.

The most noticeable discrepancy between the experimental and computed results begins to appear following the start of the upward plunge at $t/T = 0.5$. Here, the magnitude of measured lift is higher than the computed results up to $t/T = 0.8$. This discrepancy is attributed to the attachment of the plunge rods to the upper surface of the airfoil (Figure 6); the attachment is suspected of interfering with the convection of a spanwise vortex from the leading edge to trailing edge of the airfoil. The convection of this spanwise vortex is illustrated in the CFD results depicted in Frames E, F, and G ($t/T = 0.5, 0.625$, and 0.75 , respectively) in Figure 10. The interference disrupts the surface pressures at mid-span, giving rise to a higher local pressure than normal on the upper surface which, in turn, contributes to a small increment in the magnitude of the lift force from $t/T = 0.5$ to 0.8 .

5.1.2. Flowfield over the NACA 0005 airfoil

Figure 10 illustrates the flowfield over the NACA 0005 airfoil in terms of spanwise vorticity. Particle imaging

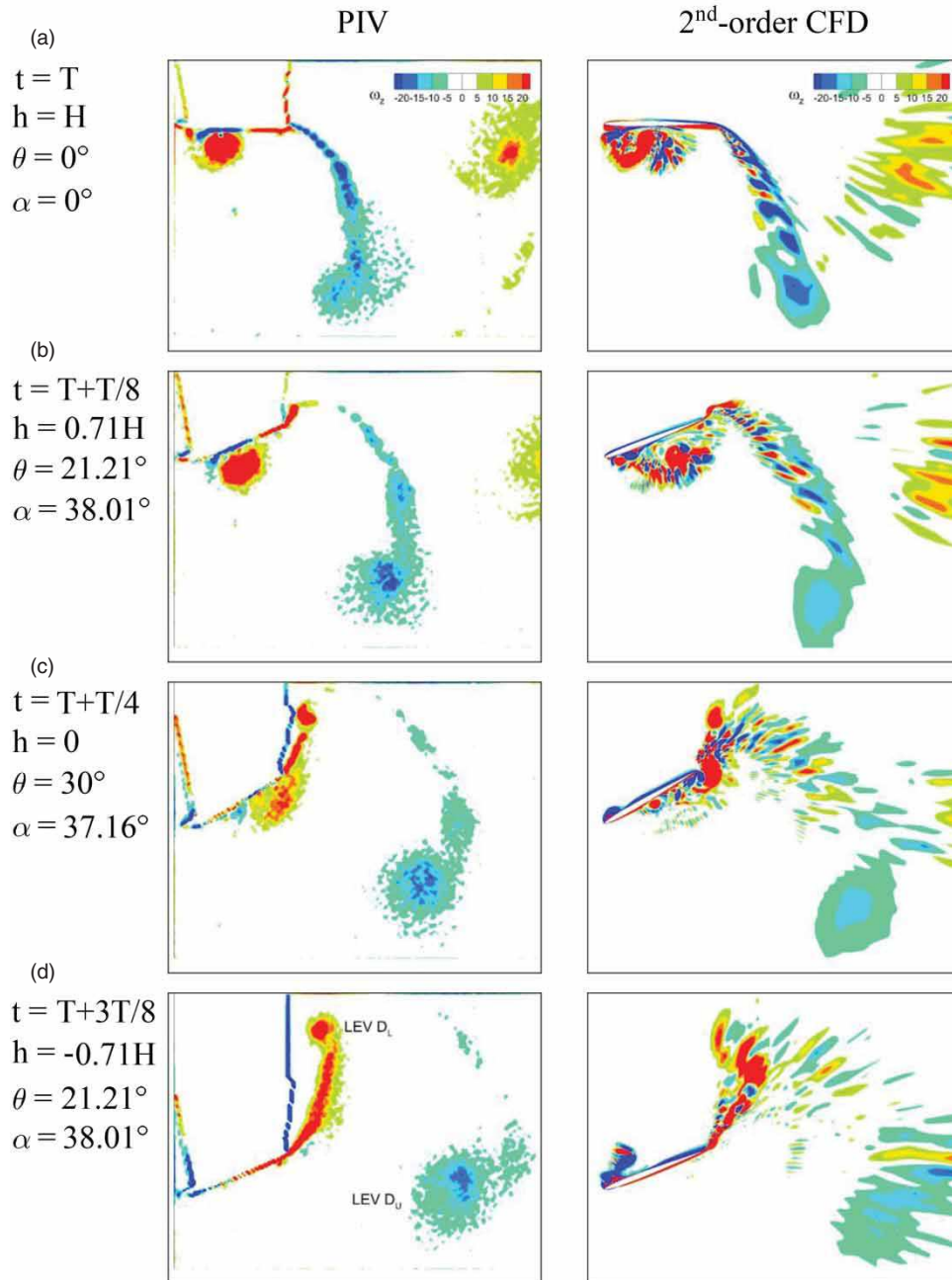


Figure 10. Downstroke: Experimental (at left) and computed spanwise vorticity (ω_z) distribution over the pitching-plunging NACA 0005 airfoil. Standard 2D test case: $Re = 10.5 \times 10^3$, $U_\infty = 0.0635$ m/s, $f = 0.5$ Hz. The temporal occurrence of each frame is identified in Figure 3. The abbreviation “LEV” represents “leading-edge vortex”; the subscripts “L” and “U” represent lower and upper surface, respectively.

velocimetry measurements and the results of CFD simulation are compared against each other at eight equally spaced points of the motion schedule as marked in Figure 9. The PIV results are an ensemble-average of 24 motion cycles; the CFD results are instantaneous and are the product of second-order calculations. Unlike the CFD simulation, PIV results for the upper surface of the airfoil are not available because the surface lay in the shadow of the laser-light sheet.

Frame A corresponds to the start of the downstroke at $t/T = 0$ as well as the end of the upstroke after Frame H. At this instant of the motion schedule, the effective angle of attack, α , is zero because the plunging velocity is zero. A vortex-pair is attached to the airfoil. The first counter-clockwise vortex (red) of this pair stands on the lower surface of the airfoil at the leading edge; the development of this vortex has its origin in the later stages of the preceding upstroke (Frames G and H). Originating from

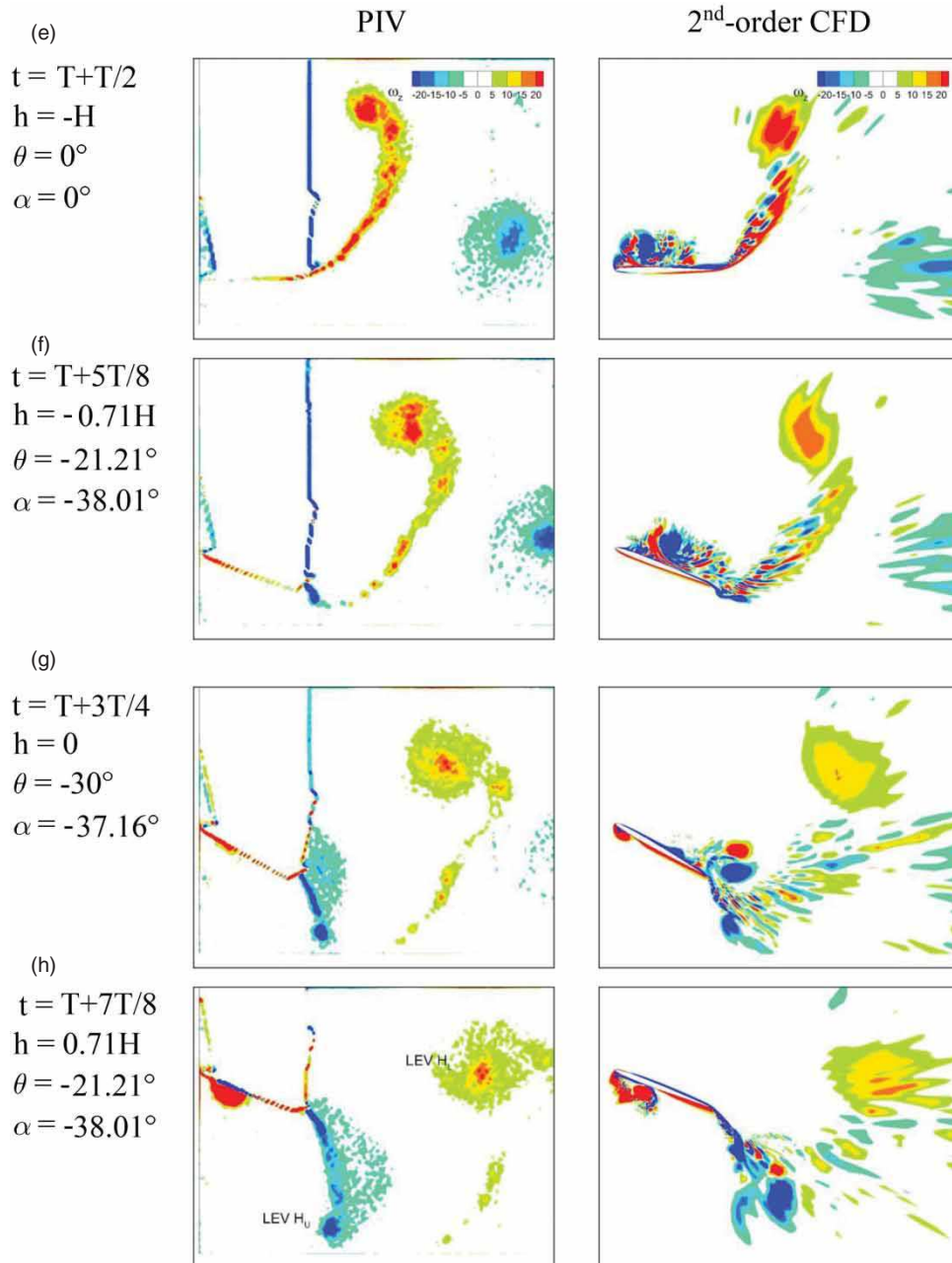


Figure 10a. Upstroke: Continued from previous page.

the upper surface of the airfoil, the second vortex (blue) of the pair is counter-rotating and has been shed from the trailing edge; however, it is considered attached because it is connected with the airfoil trailing edge through the counter-rotating vortex street and continues to receive vorticity from the airfoil. The PIV results detect a third, less intense vortex (red-yellow) downstream in the wake of the airfoil. This vortex is “free” – it does not receive vorticity from the airfoil – and is a product of the preceding cycle of motion, corresponding to the current vortex standing at the leading edge of the airfoil. In Frame B, α has passed

its first peak (Figure 3). No new vortex has formed on the upper surface owing to a phase delay. The first vortex of the pair convects along the lower surface of the airfoil; the second vortex becomes free. The free vortex downstream convects further away in the wake of the airfoil. At the instant shown in Frame C, α is midway on its approach to its second peak. Of the first pair, the first vortex has shed from the trailing edge but continues to receive vorticity from the airfoil; the second vortex continues shedding. At the leading edge of the upper surface, the first vortex (blue) of a second vortex-pair begins to emerge. By Frame

D, the airfoil is approaching the end of its downstroke. The leading-edge vortex on the upper surface continues to develop in situ. The first vortex of the first vortex-pair has shed further from the trailing edge, but still receives vorticity from the airfoil; the second vortex of the pair is convecting as a free vortex.

After examining Frames A, B, C, and D in connection with the measured and computed lift forces in Figure 9, it becomes evident that the lift force is correlated with the leading-edge vortex, but the realization of lift is phase delayed. The counter-clockwise vortex (red) on the lower surface travelling from the leading edge to the trailing edge causes the delay of lift increase, owing to the downward aerodynamic force it induces (Frames A and B). As soon as this vortex sheds from the trailing edge (Frame C), the lift begins increasing significantly. At the same time, the generation of the leading-edge vortex on the upper surface augments the lift increase. The lift reaches its maximum when this vortex takes form and begins to convect downstream.

The upstroke is represented by Frames E to H inclusive; essentially, the development of the flowfield over the airfoil is the reverse of Frames A to D, with the leading-edge vortex developing on the lower surface instead. As we have noted, the mid-span interference of the plunge rod attachment points with the convection of the upper surface vortex occurs during this portion of the motion schedule.

As demonstrated above, vortices are shed alternately from the upper and lower surfaces. The counter-clockwise rotating vortices are shed from the lower surface while the clockwise rotating vortices are shed from the upper surface; however, the shedding starts at the central (neutral) position as seen in Frames C and G for the current pitching-plunging motion. In pure plunging motion, on the other hand, according to Lai and Platzer (1999), shedding takes place when the airfoil has reached its top and bottom positions in the motion profile. This vortex shedding process forms an upper row of counter-clockwise rotating vortices and a lower row of clockwise rotating vortices in the wake, leading to a wake with velocity excess (rather than deficit) or a jet-like vortex pattern corresponding to a thrust-generating body. The thrust generation can be readily verified by the mean velocity profile in the wake (Koochesfahani, 1989). The instantaneous thrust generation will be confirmed later in Section 5.4.

It should be noted that Lai and Platzer (1999) limited the sketch of vortex shedding process at the trailing edge only. Definitive visualization of the leading-edge vortex was lacking. We clearly visualized the vortex forming on the leading edge, convecting downstream, eventually shedding from the airfoil and contributing to the jet-like vortex pattern.

In general, the flowfield around the airfoil has been simulated reasonably well by the current computations. The numerical simulation has captured successfully the

alternating development, convection, and shedding of a leading-edge vortex over both the upper and lower surfaces of the airfoil. However, there are deficiencies: first, the free vortex convecting downstream in the wake of the airfoil was not detected well; and second, in the latter stages of the downstroke (Frames C and D) and the upstroke (Frames G and H), the vorticity sheet feeding the vortex shed from the trailing edge of the airfoil was also not reproduced well. These are attributed mainly to an insufficient grid density in the second-order computations, in particular, in the region extending one chord length from the trailing edge of the airfoil into its wake. The coarse density of the grid generates numerical dissipation which tends to smear the vortex-shedding process. On the other hand, the numerical dissipation introduced by the first-order numerical scheme smeared intensively the free vortices in the wake. Nevertheless, these deficiencies did not affect the prediction of the flowfield on the airfoil surfaces and the resulting aerodynamic performance.

Earlier, we introduced the notion of an asymmetric wake. This phenomenon is illustrated in the PIV and CFD results presented in Figure 10. Consider the leading-edge vortices shed from the airfoil near the end of the downstroke (“LEV D_L ” in Frame D) and near the end of the upstroke (“LEV H_U ” in Frame H). From the PIV results, a cursory sampling of the vorticity magnitudes at the core of these vortices has revealed that the vorticity within LEV D_L is greater than the vorticity within LEV H_U by a factor of approximately two. Farther downstream in the wake, vortices LEV H_L and LEV D_U have dissipated somewhat, having comparable vorticities. Although the motion of the airfoil is symmetric, the wake it creates seemingly is not, which results in an asymmetric lift curve in time. At the end of the downstroke, vortex LEV D_L acts like a counter-clockwise circulation which induces an additional downward force on the upper surface of the airfoil. Understandably, this force is larger than the upward force induced by the vortex LEV H_U — at the end of the upstroke — causing the aforementioned asymmetry of lift in time.

Although our PIV window did not cover a wide range of the downstream wake, it is believed that the asymmetric wake has some similarities with the observations by Koochesfahani (1989) for pure pitching airfoils and by Lai and Platzer (1999) for pure plunging airfoils. They observed vortex streets in the wake region which are inclined at an angle pointing upward or downward relative to the neutral position of the airfoil. As mentioned by Lai and Platzer (1999), by applying numerical simulations, Jones, Dohring, and Platzer (1998) found that the mode of the deflected vortex street is determined by the starting condition of the plunging oscillation. Similarly, further computations in this study, starting from a mirrored or another initial flowfield solution, confirmed that the asymmetric force history is dependent on the initial solution of the flowfield.

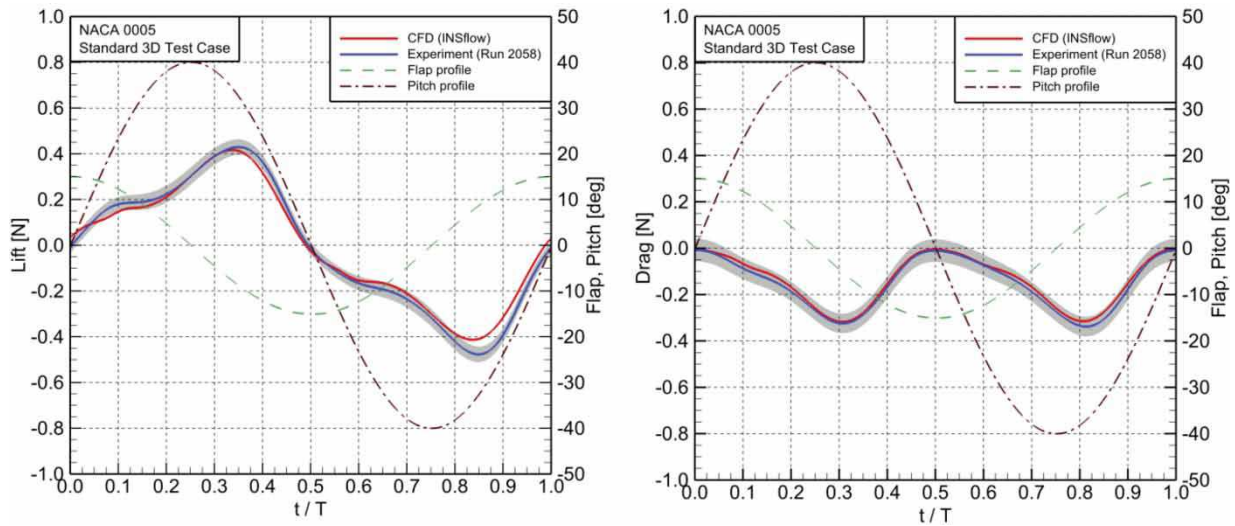


Figure 11. Measured and computed lift and drag forces for the flapping NACA 0005 wing. Standard 3D test case: $Re = 19 \times 10^3$, $U_\infty = 0.0635$ m/s, $f = 0.46$ Hz. The shaded bands represent the uncertainty in the lift and drag measurements.

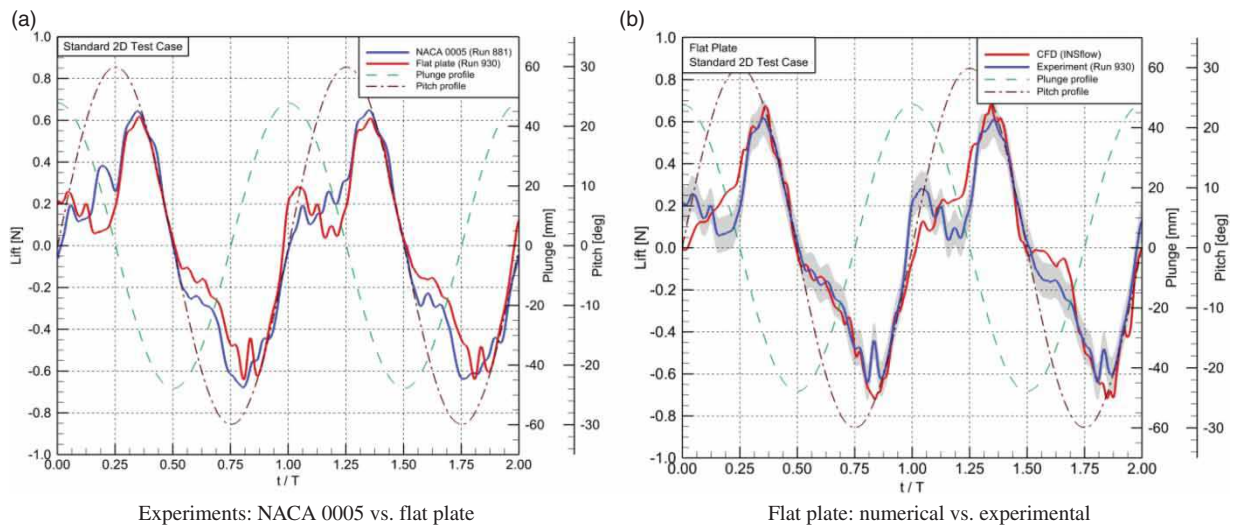


Figure 12. Lift forces for the pitching-plunging NACA 0005 airfoil. Standard 2D test case: $Re = 10.5 \times 10^3$, $U_\infty = 0.0635$ m/s, $f = 0.5$ Hz.

5.2. Standard 3D test case

One cycle of measured and computed lift and drag forces are superimposed in Figure 11. Again, the experimental results are a subset of an ensemble-average of 24 three-cycle time series; the CFD results are from the fourth cycle of a four-cycle computation. The motion profiles, again, synchronize the presentation of the two data sets. The experimental results presented here reflect a correction that was not detected prior to publication of the results elsewhere (Malhan, Lakshminarayan, Baeder, & Chopra, 2011; Yuan et al., 2010) – the correction rectifies an error in the buoyancy compensation algorithm of the data reduction process.

Similar to the results of the 2D test case, there is good agreement between the measured and computed results.

There is repeatable behavior with the flapping schedule and a phase shift between the two sets of results is not noticeable. For the most part, the computed lift force falls within the uncertainty band of lift measurement, while the computed drag force agrees very well with the drag measurement and its associated uncertainty. The peaks in the measured lift and drag forces exhibit an asymmetry in time which is attributed to the interaction of the wing model with its asymmetric wake. The computed lift and drag forces, on the other hand, are symmetric, indicating that the simulation has not captured the interaction of the wing model and an asymmetric wake, which we suspect exists based on the findings from the 2D test case. The simulation may have missed the interaction because the computed results are the product of

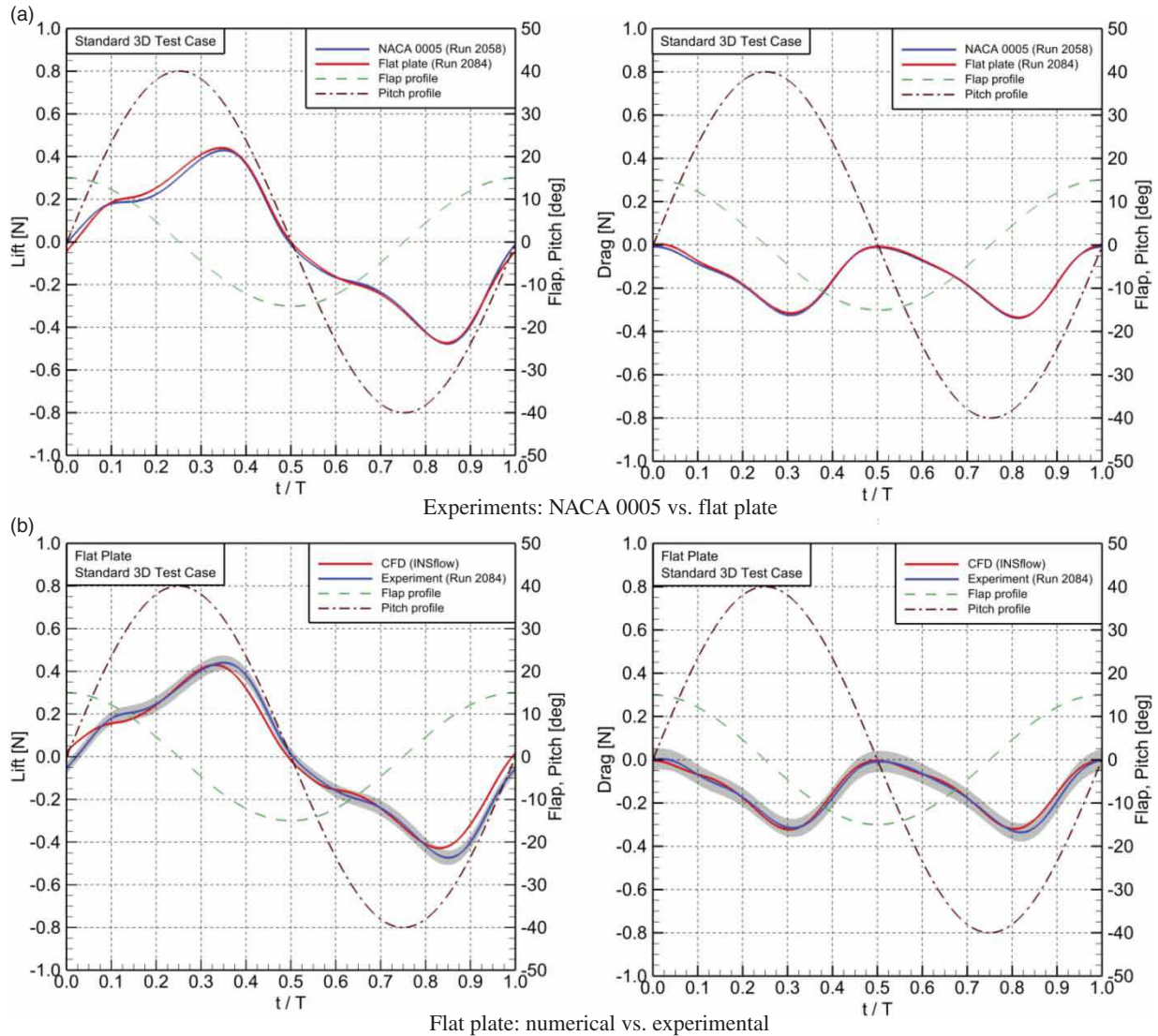


Figure 13. Lift and drag forces for the flapping NACA 0005 and flat-plate wings. Standard 3D test case: $Re = 19 \times 10^3$, $U_\infty = 0.0635$ m/s, $f = 0.46$ Hz.

first-order calculations which tended to be too dissipative.

5.3. Effect of cross-section profile

5.3.1. Standard 2D test case

The measurements of lift force acting on an airfoil with a NACA 0005 cross-sectional profile and a flat plate of constant thickness (i.e., 5% of chord) are compared in Figure 12. The two sets of results agree reasonably well, although the peak lift developed by the flat plate is slightly less than that developed by the NACA 0005 airfoil. The discrepancies between the numerical and the experimental results are also marginal. The good agreement suggests the development of aerodynamic loading is driven mainly by the kinematics of the airfoil, not its cross-sectional profile. The suggestion is founded on the general view that, in unsteady aerodynamics, lift is composed of noncirculatory

and circulatory components (Nguyen, 2008). Although the components cannot be separated from each other in this study, the current results suggest that the noncirculatory component played a dominant role in the test cases. The noncirculatory component is due to the apparent mass and inertia effects which are generated when the wing undergoes a nonzero acceleration; specifically, it is a reaction to the inertial force which develops when the fluid experiences this nonzero acceleration. The circulatory component is more important for wing sections because of the vortical intensity of circulation which generates lift (Nguyen, 2008).

5.3.2. Standard 3D test case

The measurements of lift and drag forces on wing models with a NACA 0005 cross-sectional profile and a profile of constant thickness (flat plate) are compared in Figure 13.

Similar to the 2D test case (Figure 12), the two sets of data agree very well, but the peak lift force developed by the flat-plate wing is not slightly higher. The numerical results compare well with the experimental measurements. The good agreement reinforces the earlier suggestion that the development of aerodynamic loading is influenced largely by the kinematics of the airfoil/wing.

5.4. Clap-fling effect of the wing-wing interaction

Reflection planes were used to simulate experimentally and numerically the clap-fling effect associated with the wing-to-wing interaction. The flow condition was the same as the standard 2D test case. Originally, the closest position of the reflection planes was proposed to be located at 1.0 chord from the central position of the airfoil. Due to mechanical

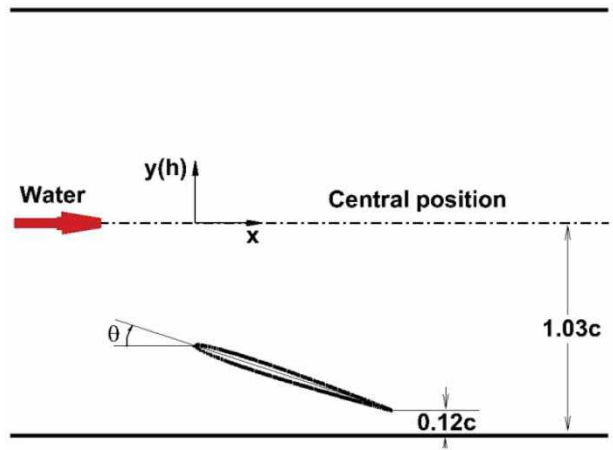


Figure 14. The setup of the reflection planes simulates clap-fling wing-wing interaction.

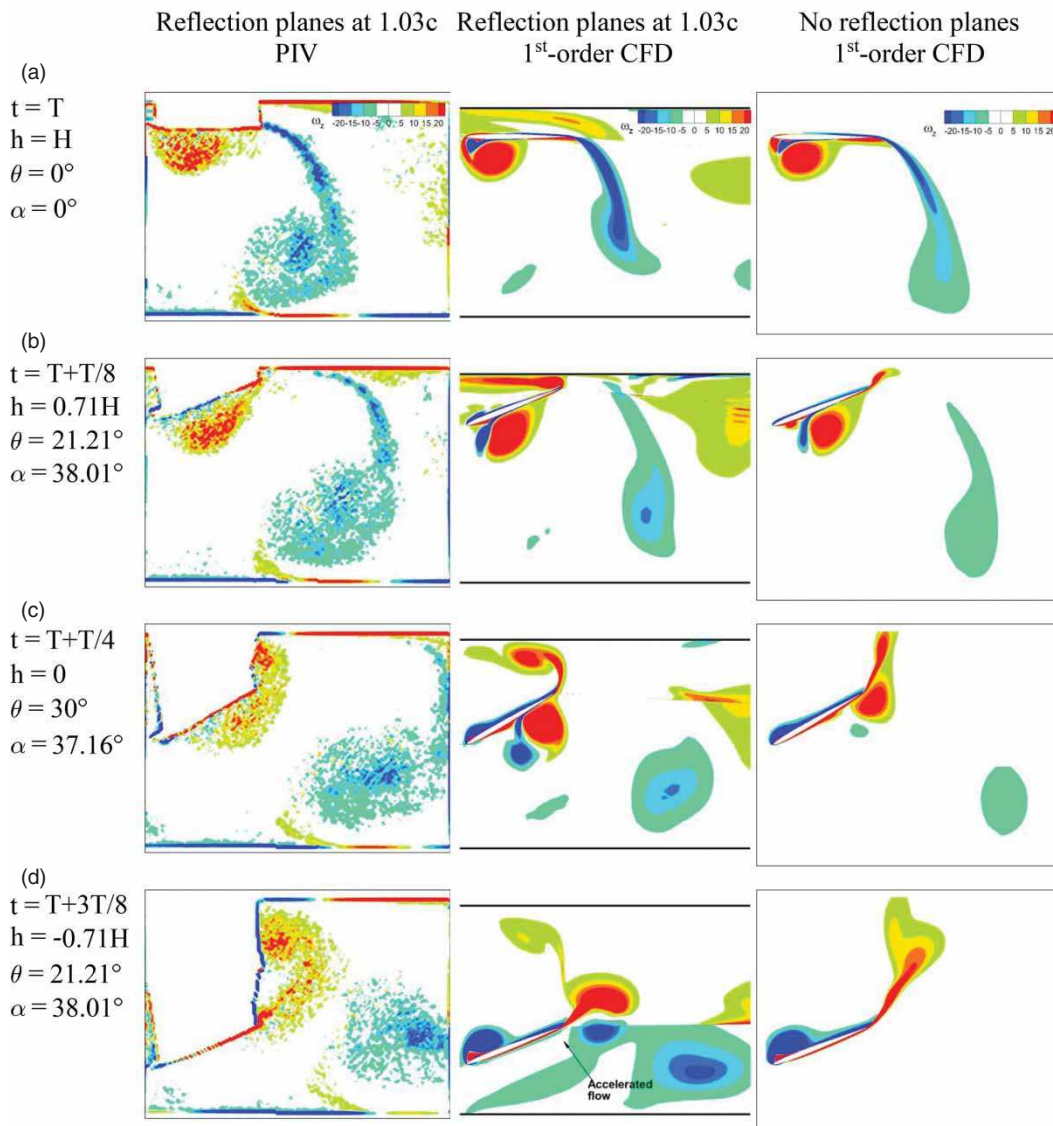


Figure 15. Downstroke: Spanwise vorticity (ω_z) distributions over the pitching-plunging NACA 0005 airfoil at $Re = 10.5 \times 10^3$.

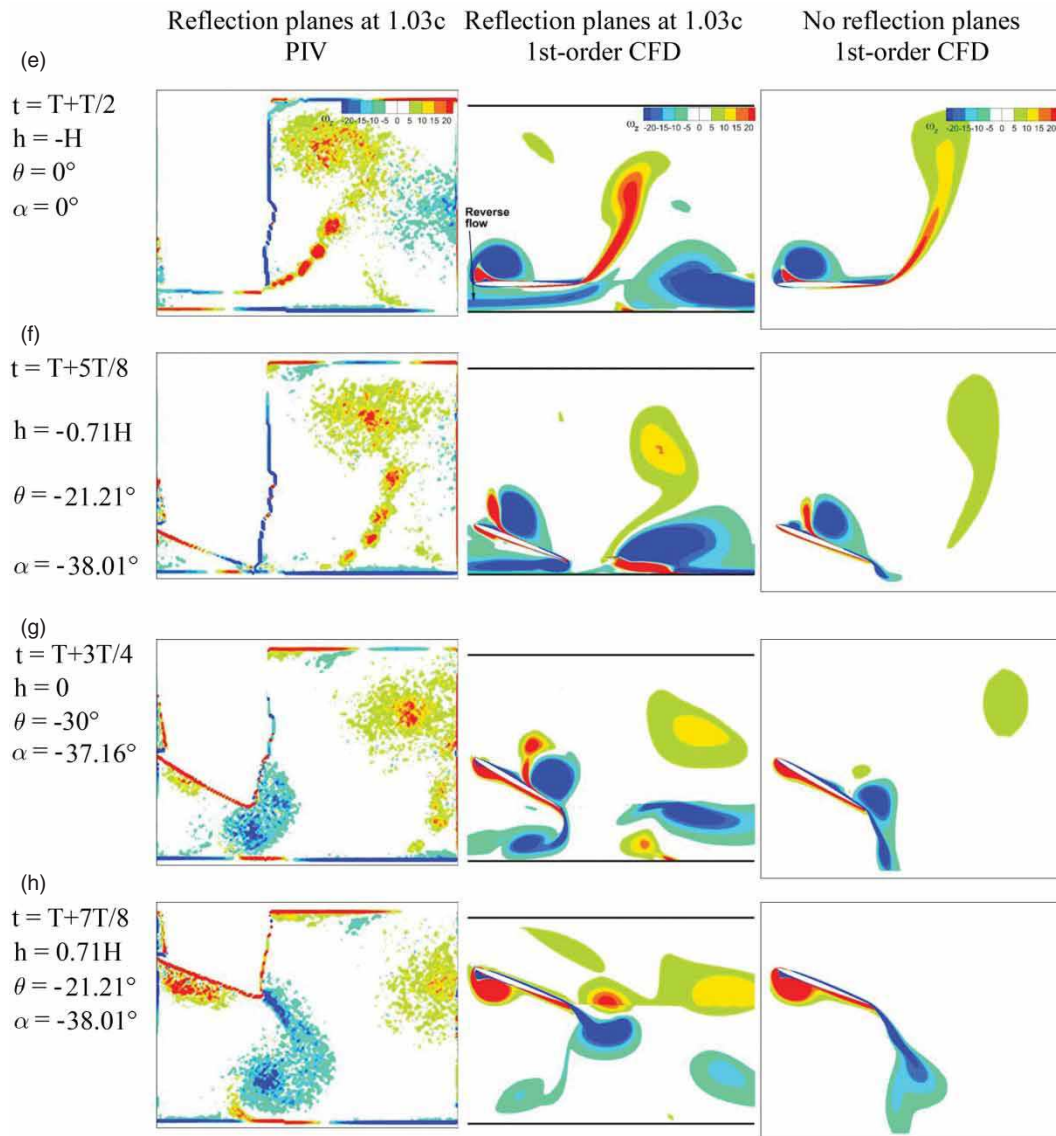


Figure 15a. Upstroke: Continued from previous page.

restrictions of the 2D motion rig and the presence of the reflection planes in the test section, the final position of the reflection planes was chosen to be $1.03c$, as shown in Figure 14. Accordingly, the closest distance between the airfoil and the reflection planes was $0.12c$ rather than originally planned $0.088c$. The longitudinal length of the reflection planes was 6 chords (38 cm) in the experiments while it was 21 chords in the CFD simulations. In the numerical simulations, the reflection planes were assumed to be symmetry planes, which indicate fully symmetric flowfields about the reflection planes or, in reality, between interacting wings. The computational domain was split into two blocks (meshes) as the upper and lower parts. Two-dimensional H-type dynamic meshes were used, which allowed for mesh deformation during the computations. Each mesh had 497×129 grid points. Laminar flow was

assumed. Since numerical instabilities were experienced in the second-order computations, results from first-order simulations are reported only.

The PIV-measured and CFD-computed flowfields of one pitching-plunging cycle are depicted in Figure 10. The PIV results are the product of an ensemble-average over 23 cycles. The CFD results presented are for an instantaneous solution. For the sake of intuitive comparisons, the first-order CFD results of the standard no-reflection-plane case are included in the right column. In the CFD simulations for the no-reflection-plane case, the third cycle produced results comparable to the second cycle; however, for the computations with the reflection planes, more than 20 cycles were needed to converge to a steady state of the periodic solution. Although there are discrepancies between the experimental and numerical results, again,

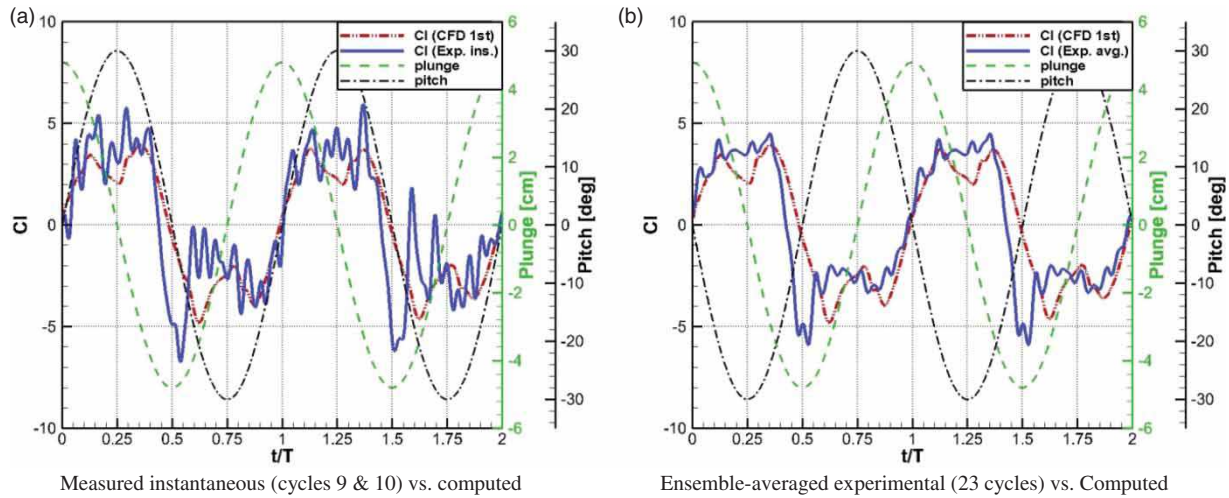


Figure 16. Computed lift coefficients compared with experimental results for the case with reflection planes located at 1.03c from the central position.

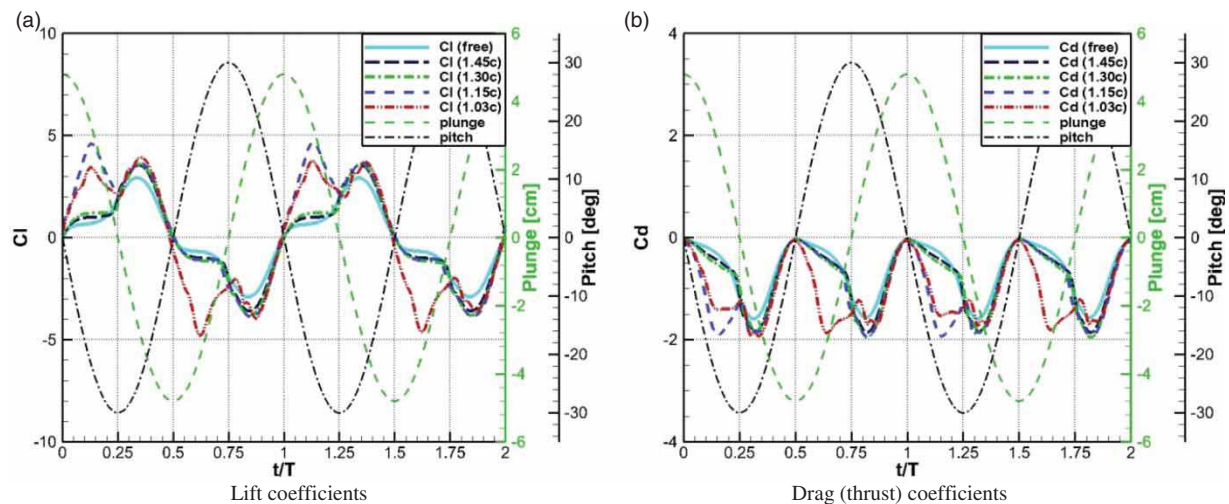


Figure 17. Effect of the proximity of the reflection plane on the lift and drag coefficients. First-order CFD results.

the first-order CFD solution captured the major physical features of vortex generation and shedding.

As shown in Figure 15, the flowfields showed some similarities to those of the test case without reflection planes. However, noticeable differences were observed:

- a) The sizes of the vortices are larger in the wing-wing interaction as compared with those in the no-reflection-plane case, suggesting that the reflection planes, or wing-wing interactions, intensify generation of the vortices.
- b) During the downstroke period of the cycle (Frame B), the clockwise-rotating leading-edge vortex (in blue) on the upper surface of the airfoil occurred earlier, compared with the no-reflection-plane condition. Furthermore, an additional counter-clockwise trailing-edge vortex (in red) was also generated on the upper surface. These features are

believed to intensify the generation of thrust, as discussed later.

- c) At the same time, it appears that suction at the upper side affects vortex shedding on the lower surface. As shown in Frames B and C, the leading-edge vortices (i.e., the counter-clockwise vortex in red on the lower surface) generated during the previous half cycle, shed slower than those in the no-reflection-plane case. In Frame C, the counter-clockwise vortex has just reached the trailing edge; at this instance in the cycle, it had already started shedding from the trailing edge at the no-reflection-plane case.
- d) When the airfoil approached the bottom reflection plane (Frame D), an accelerated flow was observed on the lower surface. The flow speed reached five times higher than the freestream speed, while it was about only three times the freestream speed

in the no-reflection-plane case. In Frame E, a flow reversal was observed between the airfoil and the reflection plane, as a result of the downwards push from the airfoil trailing edge.

Figure 16 compares the computed lift coefficient with that obtained in the experiment. While both instantaneous and ensemble-averaged experimental data are presented here, only instantaneous CFD results are depicted since the first-order CFD simulations produced a nearly periodic solution as soon as the computations converged. Although apparent discrepancies between the numerical and experimental results are noticeable, the agreement is suitable for the validation of an engineering tool.

Figure 17 further compares the effects of the reflection plane location on the aerodynamic coefficients. In general,

Table 2. Summary of the clap-fling effect in wing-wing interaction (1st-order CFD results).

Reflection plane location	Averaged drag coefficient C_d	Propulsion efficiency η_p
No planes (Freestream)	-0.64	25.4%
1.45c	-0.74	24.7%
1.30c	-0.78	24.7%
1.15c	-0.99	24.5%
1.03c	-1.08	24.6%

the reflection planes intensified the generation of the aerodynamic forces at the test conditions. The closer the reflection planes are, the stronger the observed effects. Table 2 summarizes the reflection plane effects on the thrust generation and propulsion efficiency. Negative drag coefficients

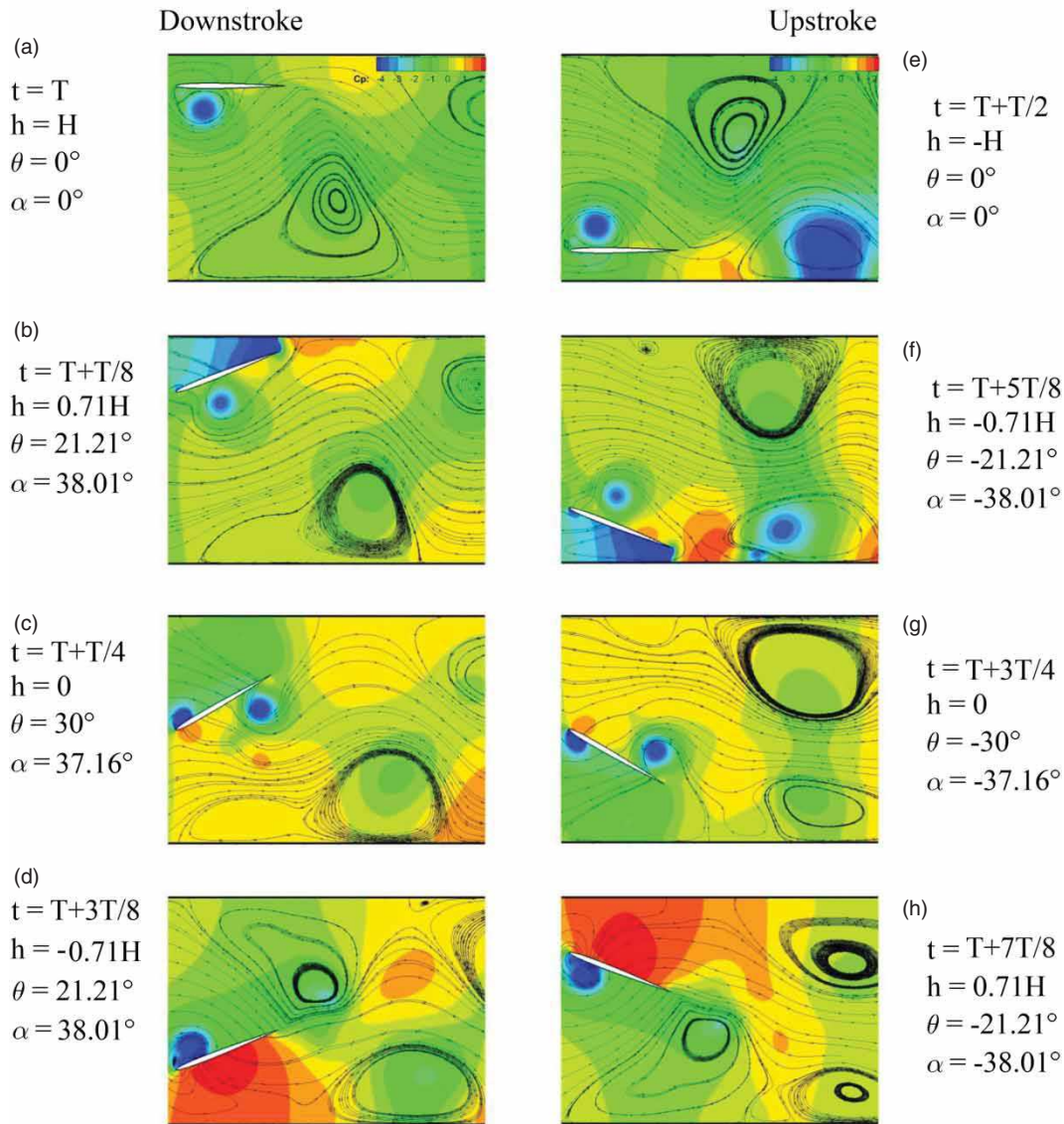


Figure 18. Computed pressure distribution and streamlines over the pitching-plunging NACA 0005 airfoil with reflection planes located at 1.03c, $Re = 10.5 \times 10^3$.

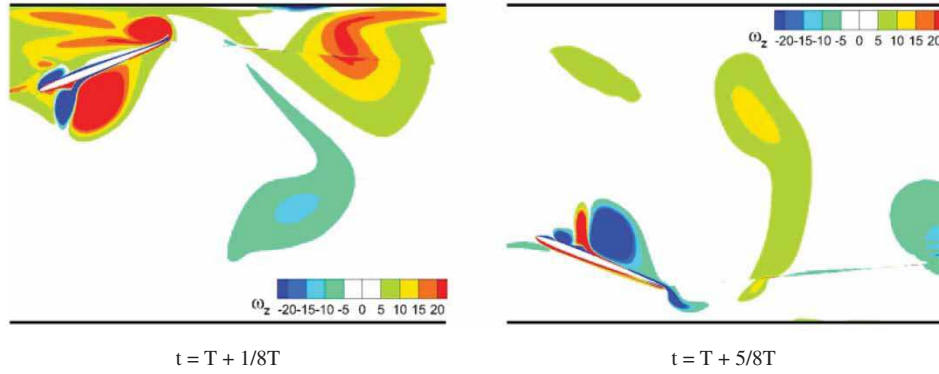


Figure 19. Computed spanwise vorticity (ω_z) distribution over the pitching-plunging NACA 0005 airfoil at $Re = 10.5 \times 10^3$, with reflection planes at 1.15c.

indicate thrust generation. As expected, the clap-fling mechanism improved the thrust generation. At the closest reflection plane placement (1.03c), the thrust coefficient is greater by 170%, compared with the no-reflection-plane case. Surprisingly, the propulsion efficiency deteriorated only slightly. For these results, the propulsion efficiency was defined as

$$\eta_p = \frac{\bar{C}_{Power,out}}{\bar{C}_{Power,in}} = \frac{-(1/TU_{ref}) \int_0^T C_d U_\infty dt}{(1/TU_{ref}) \int_0^T (C_l \dot{h} + C_m \dot{\theta} c) dt}. \quad (6)$$

This definition has countered for both the translation power input (for force acting on the airfoil) and the rotational (pitching) power input (for torque acting on the airfoil) in the denominator and is commonly used in the flapping-wing community (e.g. by Fitzgerald, Valdez, Vanella, Balaras, & Balachandran, 2011; Guglielmini & Blondeaux, 2003; Windte & Radespiel, 2008; Young & Lai, 2007). In the case when the power required for pitching motion is much smaller than that for plunging motion, the second term in the denominator can be ignored (Sunada et al., 2001). In the present study, the contribution of the pitching moment was included in the definition for completeness. However, the power input for the pitching motion was approximately 1% of the total input power.

After examining flowfield (Figure 15) in connection with the computed aerodynamic coefficients in Figure 17, it becomes evident that the augmentation of the thrust force is correlated with the vortex formation. Compared with the no-reflection-plane case, the thrust coefficient at the condition with the reflection planes located at 1.03c showed two extra peaks at $t/T = 0.125$ and 0.625 . At these time instants, the airfoil moved apart from the reflection planes (plots B and F in Figure 15) and additional vortices were generated at the trailing edge. These additional trailing-edge vortices resulted in a large area of low pressure near the trailing edge on the forward side of the airfoil (cf. plots B and F in Figure 18). This low pressure contributed significantly to the augmentation of the thrust generation.

On the other hand, when the airfoil approached the reflection planes (plots D and H in Figure 15), the accelerated flow between the airfoil and the near planes augmented also slightly to the thrust generation as shown in the thrust coefficients at $t/T = 0.25 - 0.375$ and $0.75 - 0.875$.

It is interesting that the test case with reflection planes located at 1.15c showed a completely different asymmetry with time. In Figure 17, a peak in the lift coefficient was observed clearly at $t/T = 0.125$, but not correspondingly at $t/T = 0.625$, which is different from the 1.03c case. In order to help understand the relevant flow physics or correlations, the flowfield of the selected test cases at these time instances in the cycle are illustrated in Figure 19. At $t/T = 0.125$, as the airfoil plunged downward from the upper reflection plane, leading-edge and trailing-edge vortices were observed on the upper surface of the airfoil, which is similar to that of the 1.03c case (Frame B in Figure 15). A flow reversal was also observed between the airfoil and the upper reflection plane. However, this was not the case for $t/T = 0.625$; neither the leading-edge vortex, nor the reverse flow was observed on the lower surface of the airfoil. This complex phenomenon suggests that the wings should operate in proximity close enough to another at extremes of stroke.

6. Conclusions

We have successfully performed, in a water tunnel, the standard test cases for a pitching-plunging 2D airfoil and a flapping 3D wing, as part of a collaborative partnership with DRDC Valcartier and Advanced Subsonics Inc. Force and particle imaging velocimetry measurements were carried out to acquire sets of data that are considered acceptable for the validation of corresponding CFD simulations. The experimental data have been presented specifically alongside the corresponding computational results produced by INSflow, an NRC in-house flow solver. In general there is good agreement between the experimental and numerical results. The analyses and comparisons of the

results have confirmed that our experimental approach has produced a realistic simulation. Reliable experimental data can be acquired for code validation purposes, and reliable CFD data can be generated for the development of flapping wings.

The investigation has visualized the process of vortex forming on the airfoil leading edge, convecting downstream, and eventually shedding to the wake. The visualization confirmed the major contribution of the leading-edge vortex to the reverse Karman street – a wake with velocity excess or a jet-like vortex pattern. As an ancillary finding of this research work, a perfunctory investigation of the PIV and CFD results revealed that the immediate wake of the pitching-plunging 2D airfoil is not symmetric, i.e., the leading-edge vortices of the upper and lower surfaces of the airfoil possess significantly different magnitudes of vorticity after shedding from the trailing edge. This finding has prompted the notion that these vortices, in turn, have an asymmetric influence on the loading of the airfoil. Further reflection of this notion, however, is necessary. In addition, a cross-check with the experiments has shown that further refinement of the grid in the wake region is needed, if a more accurate wake solution – in terms of resolving shed vortices — is required from the numerical simulations.

On the other hand, the kinematics of a rigid airfoil or wing – not the cross-sectional profile – is the dominant influence in the development of the lift and thrust forces, based on the current investigation. Also, the formation of the leading-edge vortex on the suction surface of the airfoil/wing augments the generation of aerodynamic forces (lift and thrust); however, the influence of vortices, connecting downstream on the pressure side of the airfoil, causes a delay in the increase of these forces.

Finally, the investigation has confirmed that the use of wing–wing interaction, known as the clap-fling effect (Ellington, 1984), intensifies the generation of the aerodynamic forces. The augmentation of the thrust generation is mainly due to the formation of the trailing-edge vortices in addition to the leading-edge ones, when they peel apart. To realize the clap-fling effect, flapping wings should operate in close proximity to another at extremes of stroke.

Facilitating the desired approach to measure the drag force for 2D test cases and PIV techniques for 3D test cases would further help improving the data quality and elucidating the insights of flow physics. Further studies on the wake flow, including signal spectrum analysis, would help quantify the contribution from both leading-edge and trailing-edge vortices to the reverse Karman vortex street.

Acknowledgments

The authors wish to thank Francois Lesage of DRDC Valcartier – for his leadership and management of the collaboration – and the Technology Investment Fund (TIF) from Department of National Defence Canada. We are also thankful for the meaningful discussions with other members of the team, namely

Patrick Zdunich (formerly of Advanced Subsonics, currently of the Flight Research Laboratory at the NRC) and Nicolas Hamel (DRDC Valcartier). Patrick's role as the diligent custodian of the standard test cases was greatly appreciated. Special thanks are also given to our colleagues at the NRC: Dr. Stuart McIlwain, who has played a supervision role in the early stage of the experimental preparation; Pierre Gravelle, who assembled, wired and calibrated the bi-fold five-component balance; and Alain Bilodeau, for the excellent craftsmanship he invested in the fabrication of the two-dimensional airfoil and three-dimensional wing models.

References

- Azuma, A., Okamoto, M., & Yasuda, K. (2001). Aerodynamic characteristics of wings at low Reynolds number. In T. J. Muell (Ed.), *Fixed and flapping wing aerodynamics for micro air vehicle applications* (pp. 341–398). Reston, VA: American Institute of Aeronautics and Astronautics.
- Betz, A. (1912). Ein Beitrag zur Erklarung des Segelfluges. *Zeitschrift fuer Flugtechnik und Motorluftschiffahrt*, 3(21), 269–272.
- Chorin, A. J. (1968). Numerical solution of the Navier-Stokes equations. *Mathematics of Computation*, 22: 745–762.
- DeLaurier, J. D. (1993a). An aerodynamic model for flapping-wing flight. *The Aeronautical Journal*, 97(964), 125–130.
- DeLaurier, J. D. (1993b). The development of an efficient ornithopter wing. *The Aeronautical Journal*, 97(965), 153–162.
- Demirdžić, I., & Perić, M. (1990). Finite volume method for prediction of fluid flow in arbitrarily shaped domains with moving boundaries. *International Journal for Numerical Methods in Fluids*, 10, 771–790.
- Dickinson, M. H., Lehmann, F. O., & Sane, S. P. (1999). Wing rotation and the aerodynamic basis of insect flight. *Science*, 284: 1954–1960.
- Ellington, C. P. (1984). The aerodynamics of hovering insect flight. *Philosophical Transactions of the Royal Society of London, Ser. B Biological Sciences*, 305(1122), 79–113.
- Fairuz, Z. M., Abdullah, M. Z., Yusoff, H., & Abdullah, M. K. (2014). Fluid structure interaction of unsteady aerodynamics of flapping wing at low Reynolds number. *Engineering Applications of Computational Fluid Mechanics*, 7(1), 144–158.
- Ferziger, J. H., & Perić, M. (1996). *Computational methods for fluid dynamics*. Berlin: Springer-Verlag.
- Fitzgerald, T., Valdez, M., Vanella, M., Balaras, E., & Balachandran, B. (2011). Flexible flapping system: computational investigations into fluid-structure interactions. *The Aeronautical Journal*, 115(1172), 593–603.
- Freymuth, P. (1990). Thrust generation by an airfoil in hover modes. *Experiments in Fluids*, 9(1), 17–24.
- Guglielmini, L., & Blondeaux, P. (2003). Propulsive efficiency of oscillating foils. *European Journal of Mechanics B/Fluids*, 23, 255–278.
- Hall, K., Pigott, S., & Hall, S. (1997, January 6–9). *Power requirements for large-amplitude flapping flight*. Proceedings of 35th AIAA Aerospace Sciences Meeting & Exhibit, Reno, NV, AIAA paper 1997–0827.
- Hall, K., & Hall, S. (2001). A rational engineering analysis of the efficiency of flapping flight. In T. J. Mueller (Ed.), *Fixed and flapping wing aerodynamics for micro air vehicle applications* (pp. 249–274). Reston, VA: American Institute of Aeronautics and Astronautics.

- Isaac, K. M., Rolwes, J., & Colozza, A. (2008). Aerodynamics of flapping and pitching wing using simulations and experiments. *AIAA Journal*, 46(6), 1505–1515.
- Jones, K. D., Dohring, C. M., & Platzer, M. P. (1998). Experimental and computational investigation of the Knoller–Betz effect. *AIAA Journal*, 36(7), 1240–1246.
- Knoller, R. (1909). Die Gesetze des Luftwiderstandes. *Flug- und Motortechnik (Wien)*, 3(21), 1–7.
- Koochesfahani, M. (1989). Vortical patterns in the wake of an oscillating airfoil. *AIAA Journal*, 27(9), 1200–1205.
- Lai, J. C. S., & Platzer, M. F. (1999). Jet characteristics of a plunging airfoil. *AIAA Journal*, 37(12), 1529–1537.
- Lai, J. C. S., & Platzer, M. F. (2001). Characteristics of a plunging airfoil at zero freestream velocity. *AIAA Journal*, 39(3), 531–534.
- Lee, R., Yuan, W., Levasseur, L., & Hoogkamp, E. (2011, June 27–30). *Experimental simulation of flapping wings for nano-air-vehicles*. Proceedings of 29th AIAA Applied Aerodynamics Conference, Honolulu, Hawaii, AIAA paper 2011–3790.
- Lesage, F., Hamel, N., Yuan, W., Khalid, M., Huang, X., & Zdunich, P. (2008, August 18–21). *Aerodynamic study of a flapping-wing NAV using a combination of numerical and experimental methods*. Proceedings of 26th AIAA Applied Aerodynamics Conference, Hawaii, AIAA 2008–6396.
- Liu, H., Ellington, C. P., Kawachi, K., van Den Berg, C., & Willmott, A. P. (1998). A computational fluid dynamic study of hawkmoth hovering. *The Journal of Experimental Biology*, 201, 461–477.
- Liu, H., & Kawachi, K. (1998). A numerical study of insect flight. *Journal of Computational Physics*, 146, 124–156.
- Malhan, R., Lakshminarayan, V. K., Baeder, J., & Chopra, I. (2011, January 25–27). *Investigation of aerodynamics of rigid flapping wings for MAV applications: CFD validation*. Proceedings of AHS Specialists Conference of the American Helicopter Society, Tempe, Arizona.
- Mueller, T. J. (2001). *Fixed and flapping wing aerodynamics for micro air vehicle applications*. Reston, VA: American Institute of Aeronautics and Astronautics.
- Nguyen, N. (2008, January 7–10). *Integrated flight dynamic modeling of flexible aircraft with inertial force-propulsion-aeroelastic coupling*. Proceedings of 46th AIAA Aerospace Sciences Meeting and Exhibit, Reno, NV, AIAA paper 2008–194.
- Ol, M. (2010). *AVT-149 task group. Unsteady aerodynamics for micro air vehicles* (Final Report of Task Group AVT-149, RTO Technical Report). North Atlantic Treaty Organization.
- Patankar, S. V. (1980). *Numerical heat transfer and fluid flow*. Washington: Hemisphere Publishing Corporation.
- Platzer, M., Jones, K., Young, J., & Lai, J. (2008). Flapping-wing aerodynamics: progress and challenges. *AIAA Journal*, 46(9), 2136–2149.
- Sane, S. P., & Dickinson, M. H. (2001). The control of flight force by a flapping wing: lift and drag production. *The Journal of Experimental Biology*, 204, 2607–2626.
- Shyy, W., Lian, Y., Tang, J., Viieru, D., & Liu, H. (2008). *Aerodynamics of low Reynolds number flyers*. New York: Cambridge University Press.
- Sunada, S., Kawachi, K., Matsumoto, A., & Sakaguchi, A. (2001). Unsteady forces on a two-dimensional wing in plunging and pitching motions. *AIAA Journal*, 39(7), 1230–1239.
- Weis-Fogh, T. (1973). Quick estimates of flight fitness in hovering animals, including novel mechanisms for lift production. *Journal of Experimental Biology*, 59, 169–230.
- Windte, J., & Radespiel, R. (2008). Propulsive efficiency of a moving airfoil at transitional low Reynolds numbers. *AIAA Journal*, 40(9), 2165–2177.
- Young, J. (2005). *Numerical simulation of the unsteady aerodynamics of flapping airfoils* (PhD thesis, School of Aerospace, Civil and Mechanical Engineering). New South Wales: The University of New South Wales, Australian Defence Force Academy.
- Young, J., & Lai, J. (2007). Mechanisms influencing the efficiency of oscillating airfoil propulsion. *AIAA Journal*, 45(7), 1695–1702.
- Young, J., Lai, J. C. S., & Germain, C. (2008). Numerical simulation and parameter variation of insect wing motion based on dragonfly hovering. *AIAA Journal*, 46(4), 918–924.
- Yuan, W., Khalid, M., Windte, J., Scholz, U., & Radespiel, R. (2007). Computational and experimental investigations of low-Reynolds-number flows past an airfoil. *The Aeronautical Journal*, 111(1115), 17–29.
- Yuan, W., & Khalid, M. (2008). Preliminary CFD studies of flapping-wing aerodynamics. *Canadian Aeronautics and Space Journal*, 54(3/4), 51–63.
- Yuan, W., Khalid, M., & Huang, X. (2008, August 18–21). *Computations of flows past an insect-like flapping wing*. Proceedings of 26th AIAA Applied Aerodynamics Conference, Hawaii, AIAA 2008–6395.
- Yuan, W., Lee, R., Hoogkamp, E., & Khalid, M. (2010). Numerical and experimental simulations of flapping wings. *International Journal of Micro Air Vehicles*, 2(3), 181–209.
- Yuan, W., Poirel, D., & Wang, B. (2013). Simulations of pitch-heave limit-cycle oscillations at a transitional Reynolds number. *AIAA Journal*, 51(7), 1716–1732.
- Yuan, W., Poirel, D., Wang, B., & Benaissa, A. (2014). Effect of freestream turbulence on airfoil limit-cycle oscillations at transitional Reynolds numbers. *Journal of Aircraft*. Advanced online publication. doi:10.2514/1.C032807.
- Zdunich, P., Bilyk, D., MacMaster, M., Loewen, D., DeLaurier, J., Kornbluh, R., Low, T., Stanford, S., & Holeman, D. (2007). Development and testing of the Mentor flapping-wing micro air vehicle. *Journal of Aircraft*, 44(5), 1708–1711.
- Zdunich, P. (2008, August 18–21). *Separated-flow discrete vortex model for nano-scale hovering flapping wings*. Proceedings of 26th AIAA Applied Aerodynamics Conference, Hawaii, AIAA 2008–6245.
- Zdunich, P. (2010). *Development and application of a 3D vortex panel model with leading edge separation suitable for hovering flapping-wing flight* (Technical Report). Montreal: Advanced Subsonics.